14

Study of Hydrodynamics and Heat Transfer in the Fluidized Bed Reactors

Mahdi Hamzehei
Islamic Azad University, Ahvaz Branch, Ahvaz
Iran

1. Introduction

Fluidized bed reactors are used in a wide range of applications in various industrial operations, including chemical, mechanical, petroleum, mineral, and pharmaceutical industries. Fluidized multiphase reactors are of increasing importance in nowadays chemical industries, even though their hydrodynamic behavior is complex and not yet fully understood. Especially the scale-up from laboratory towards industrial equipment is a problem. For example, equations describing the bubble behavior in gas-solid fluidized beds are (semi) empirical and often determined under laboratory conditions. For that reason there is little unifying theory describing the bubble behavior in fluidized beds.

Understanding the hydrodynamics of fluidized bed reactors is essential for choosing the correct operating parameters for the appropriate fluidization regime. Two-phase flows occur in many industrial and environmental processes. These include pharmaceutical, petrochemical, and mineral industries, energy conversion, gaseous and particulate pollutant transport in the atmosphere, heat exchangers and many other applications. The gas–solid fluidized bed reactor has been used extensively because of its capability to provide effective mixing and highly efficient transport processes. Understanding the hydrodynamics and heat transfer of fluidized bed reactors is essential for their proper design and efficient operation. The gas–solid flows at high concentration in these reactors are quite complex because of the coupling of the turbulent gas flow and fluctuation of particle motion dominated by inter-particle collisions. These complexities lead to considerable difficulties in designing, scaling up and optimizing the operation of these reactors [1-3].

Multiphase flow processes are key element of several important technologies. The presence of more than one phase raises several additional questions for the reactor engineer. Multiphase flow processes exhibit different flow regimes depending on the operating conditions and the geometry of the process equipment. Multiphase flows can be divided into variety of different flows. One of these flows in gas-solid flows. In some gas-solid reactors (fluidized reactors); gas is the continuous phase and solid particles are suspended within this continuous phase. Depending on the properties of the gas and solid phases, several different sub-regimes of dispersed two-phase flows may exist. For relatively small gas flow rates, the rector may contain a dense bed of fluidized solid particles. The bed may be homogenously fluidized or gas may pass through the bed in the form of large bubbles. Further increase in gas flow rate decreases the bed density and the gas-solid contacting pattern may change from dense bed to turbulent bed, then to fast-fluidized mode and ultimately to pneumatic conveying mode. In all these flow regimes the relative importance

of gas-particle, particle-particle, and wall interaction is different. It is, therefore necessary to identify these regimes to select an appropriate mathematical model. Apart from density and particle size as used in Geldart's classification, several other solid properties, including angularity, surface roughness and composition may also significantly affect quality of fluidization (Grace, 1992). However, Geldart's classification chart often provides a useful starting point to examine fluidization quality of a specific gas-solid system. Reactor configuration, gas superficial velocity and solids flux are other important parameters controlling the quality of fluidization. At low gas velocity, solids rest on the gas distributor and the regime is a fixed bed regime. The relationship between some flow regimes, type of solid particles and gas velocity is shown schematically in Fig.1. When superficial gas velocity increases, a point is reached beyond which the bed is fluidized. At this point all the particles are just suspended by upward flowing gas. The frictional force between particle and gas just counterbalances the weight of the particle.

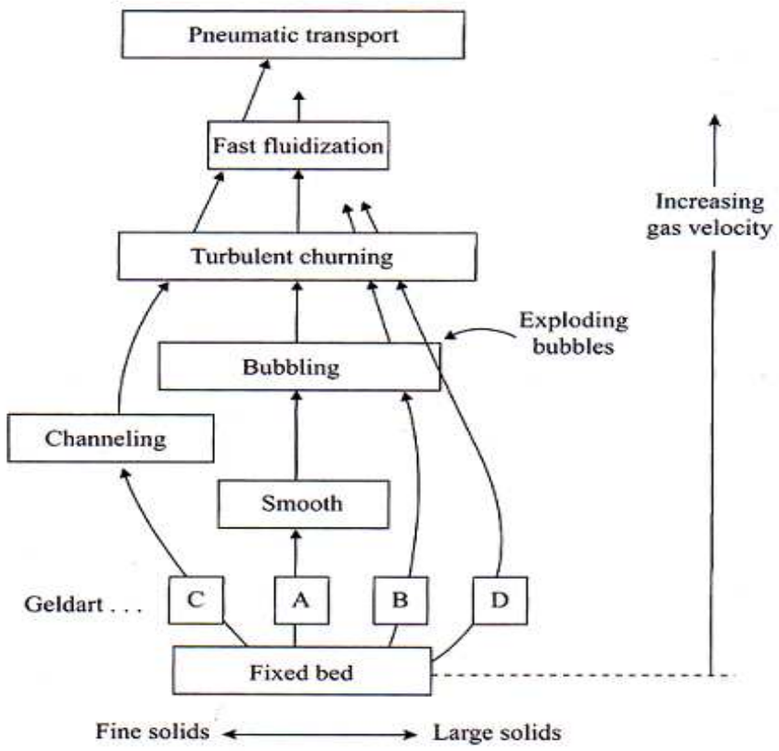

Fig. 1. Progressive change in gas-solid contact (flow regimes) with change on gas velocity

This gas velocity at which fluidization begins is known as minimum fluidization velocity (U_{mf}) the bed is considered to be just fluidized, and is referred to as a bed at minimum fluidization. If gas velocity increases beyond minimum fluidization velocity, homogeneous (or smooth) fluidization may exist for the case of fine solids up to a certain velocity limit. Beyond this limit (U_{mb} : minimum bubbling velocity), bubbling starts. For large solids, the bubbling regime starts immediately if the gas velocity is higher than minimum fluidization velocity ($U_{mb} = U_{mf}$). With an increase in velocity beyond minimum bubbling velocity, large instabilities with bubbling and channeling of gas are observed. At high gas velocities, the movement of solids becomes more vigorous. Such a bed is called a bubbling bed or

heterogeneous fluidized bed, in this regime; gas bubbles generated at the distributor coalesce and grow as they rise through the bed. For deep beds of small diameter, these bubbles eventually become large enough to spread across the diameter of the vessel. This is called a slugging bed regime. In large diameter columns, if gas velocity increases still further, then instead of slugs, turbulent motion of solid clusters and voids of gas of various size and shape are observed, Entrainment of solids becomes appreciable. This regime is called a turbulent fluidized bed regime. With further increase in gas velocity, solids entrainment becomes very high so that gas-solid separators (cyclones) become necessary. This regime is called a fast fluidization regime. For a pneumatic transport regime, even higher gas velocity is needed, which transports all the solids out of the bed. As one can imagine, the characteristics of gas-solid flows of these different regimes are strikingly different. It is, therefore, necessary to determine the prevailing flow regime in order to select an appropriate mathematical model to represent it.

Computational fluid dynamics (CFD) offers an approach to understanding the complex phenomena that occur between the gas phase and the particles. With the increased computational capabilities, computational fluid dynamics (CFD) has become an important tool for understanding the complex phenomena that occur between the gas phase and the particles in fluidized bed reactors [3, 4, 5]. As a result, a number of computational models for solving the non-linear equations governing the motion of interpenetrating continua that can be used for design and optimization of chemical processes were developed. Two different approaches have been developed for application of CFD to gas–solid flows, including the fluidized beds. One is the Eulerian-Lagrangian method where a discrete particle trajectory analysis method based on the molecular dynamics model is used which is coupled with the Eulerian gas flow model. The second approach is a multi-fluid Eulerian–Eulerian approach which is based on continuum mechanics treating the two phases as interpenetrating continua. The Lagrangian model solves the Newtonian equations of motion for each individual particle in the gas-solid system along with a collision model to handle the energy dissipation caused by inelastic particle-particle collision. The large number of particles involved in the analysis makes this approach computationally intensive and impractical for simulating fluidized bed reactors at high concentration. The Eulerian model treats different phases as interpenetrating and interacting continua. The approach then develops governing equations for each phase that resembles the Navier-Stokes equations. The Eulerian approach requires developing constitutive equations (closure models) to close the governing equations and to describe the rheology of the gas and solid phases.

For gas-solid flows modeling, usually, Eulerian-Lagrangian are called discrete particle models and Eulerian-Eulerian models are called granular flow models. Granular flow models (GFM) are continuum based and are more suitable for simulating large and complex industrial fluidized bed reactors containing billions of solid particles. These models, however, require information about solid phase rheology and particle-particle interaction laws. In principle, discrete particle models (DPM) can supply such information. DPMs in turn need closure laws to model fluid-particle interactions and particle-particle interaction parameters based on contact theory and material properties. In principle, it is possible to work our way upwards from direct solution of Navier-Stokes equations. Lattice-Boltzmann models and contact theory to obtain all the necessary closure laws and other parameters required for granular flow models. However, with the present state of knowledge, complete a priori simulations are not possible. It is necessary to use these different models judiciously. Combined with key experiments, to obtain the desired engineering information about

gas-solid flows in industrial equipment. Direct solution of Navier-Stokes equations or lattice Boltzmann methods are too computation intensive to simulate even thousands of solid particles. Rather than millions of particles, DPMs are usually used to gain an insight into various vexing issues such as bubble or cluster formations and their characteristics or segregation phenomena. A few hundred thousand particles can be considered in such DPMs.

The kinetic theory of granular flow that treats the kinetic energy of the fluctuating component of the particle velocity as the granular temperature has been used to guide the development of appropriate constitutive laws [3, 4]. In particular, solid pressure and effective viscosity of the particulate phase were successfully predicted from the kinetic theory of granular materials. Simulations of the hydrodynamics of gas-solid multiphase systems with the Eulerian models using different CFD codes have shown the suitability of the approach for modeling fluidized bed reactors [5, 6]. The reduced number of equations that need to be solved is the main advantage of the Eulerian approach in comparison with the Lagrangian method.

The fundamental problem encountered modeling of these reactors is the motion of two phases where the interface is unknown and transient, and the interaction is understood only for a limited range of conditions. Also, a large number of independent variables such as particle density, size and shape can influence hydrodynamic behavior [2,3,5]. Despite a significant amount of research on fluidized bed reactors, there are considerable uncertainties on their behavior. Part of the confusion is due to the presence of various complex flow regimes and their sensitivities to the operating conditions of these reactors. The fundamental problem encountered in modeling the hydrodynamics of a gas–solid fluidized bed is the strong interaction of the phases with unknown and transient interfaces. As a result, the interaction of the phases is understood only for a limited range of conditions. One additional important complexity is that in many of these industrial processes the gas flow is in a turbulent state of motion [2,3,5].

Recently, Nasr and Ahmadi [7] studied the turbulence modulation due to the presence of dispersed solid particles in a downward, fully developed channel flow. The Eulerian framework was used for the gas phase, whereas the modified Lagrangian approach was used for the particle-phase. The steady-state equations of conservation of mass and momentum were used for the gas phase, and the effect of turbulence was included via a $k-\varepsilon$ model. Taghipour et al. [8] have conducted experimental and computational studies of hydrodynamics of gas–solid flows in a fluidized bed reactor. The simulation results were compared with the experimental data. The model predicted bed expansion and gas–solid flow patterns reasonably well. Furthermore, the predicted instantaneous and time-average local voidage profiles showed trends similar to the experimental data. A multi fluid Eulerian model integrating the kinetic theory for solid particles was used of predicting the gas–solid behavior of a fluidized bed. Comparison of the model predictions, using the Syamlal–O'Brien, Gidaspow, and Wen–Yu drag functions, and experimental measurements on the time-average bed pressure drop, bed expansion, and qualitative gas–solid flow pattern indicated reasonable agreement for most operating conditions. Furthermore, the predicted instantaneous and time-average local voidage profiles showed similar trends with the experimental results.

Kaneko et al. [9] numerically analyzed temperature behavior of particles and gas in a fluidized bed reactor by applying a discrete element method, where heat transfer from particles to the gas was estimated using Ranz–Marshall equation. CFD simulation of a

fluidized bed reactor was also conducted by Rong et al. [10] focusing on the chemical kinetic aspects and taking into account the intra-particle heat and mass transfers, poly-disperse particle distributions, and multiphase fluid dynamics. Gas–solid heat and mass transfer, polymerization chemistry and population dynamic equations were developed and solved in a multi-fluid code (MFIX) in order to describe particle growth.

Behjat et al. [11] investigated unsteady state behavior of gas–solid fluidized beds. They showed that the model predictions of bubble size and gas–solid flow pattern using both Syamlal–O'Brien and Gidaspow drag models were similar. Also, when the bed containing two different solid phases was simulated, the results showed particles with smaller diameters had lower volume fraction at the bottom of the bed and higher volume fraction at the top of the reactor.

Gobin et al. [12] numerically simulated a fluidized bed using a two-phase flow method. In their study, time-dependent simulations were performed for industrial and pilot reactor operating conditions. Their numerical predictions were in qualitative agreement with the observed behavior in terms of bed height, pressure drop and mean flow regimes. Wachem et al. [13,14,15] verified experimentally their Eulerian-Eulerian gas-solid simulations of bubbling fluidized beds with existing correlations for bubble size or bubble velocity. A CFD model for a free bubbling fluidized bed was implemented in the commercial code CFX. This CFD model was based on a two-fluid model including the kinetic theory of granular flows. Chiesa et al. [16] have presented a computational study of the flow behavior of a lab-scale fluidized bed. The results obtained from a 'discrete particle method' (DPM) were qualitatively compared with the results obtained from a multi-fluid computational fluid dynamic (CFD) model. They have also compared the experimental data for bubble formation with their computational results. The results obtained from the Eulerian - Lagrangian approach were found to show a much better agreement with the experimental data than those that were obtained by the Eulerian-Eulerian approach.

Mansoori et al. [17] investigated thermal interaction between a turbulent vertical gas flow and particles injected at two different temperatures experimentally and numerically. A two-phase $k-\tau$ and $k_\theta-\tau_\theta$ numerical model in four-way coupled simulation was used in a Eulerian-Lagrangian framework. In agreement with the numerical results, the experiments showed that the addition of hot particles to the suspension can cause an increase in the heat transfer coefficient. Also, in another paper [18] they used their four-way Eulerian-Lagrangian formulation to study the particle–particle heat transfer in turbulent gas–solid flows in a riser. Their formulation included the particle–particle collisions, in addition to the $k-\tau$ and the $k_\theta-\tau_\theta$ model equations. To examine the nature of inter-particle heat transfer, two groups of particles with different temperatures were fed into the flow field. Their numerical simulations included an inelastic soft sphere collision model, but unsteadiness and variation of gas velocity in the gas lens between two colliding particles and the non-continuum effects were neglected. Validations of the predicted velocity and heat transfer were also presented in [18]. Saffar-Avval et al. [19] performed simulations of gas–solid turbulent upward flows in a vertical pipe using the Eulerian–Lagrangian approach. Particle–particle and particle–wall collisions were simulated using a deterministic collision model. The influence of particle collisions on the particle concentration, mean temperature and fluctuating velocities was investigated. Numerical results were presented for different values of mass loading ratios. The profiles of particle concentration, mean velocity and temperature were shown to be flatter by considering inter-particle collisions, while this

effect on the gas mean velocity and temperature was not significant. It was demonstrated that the effect of inter-particle collisions had a dramatic influence on the particle fluctuation velocity.

Despite many studies on the modeling and model evaluation of fluidized-bed hydrodynamics, only a few works have been published on the CFD modeling and model validation of combined reactor hydrodynamics and heat transfer [1-50]. For example, Huilin et al. [28, 38] studied bubbling fluidized bed with the binary mixtures applying multi-fluid Eularian CFD model according to the kinetic theory of granular flow. Their simulation results showed that hydrodynamics of gas bubbling fluidized bed are related with the distribution of particle sizes and the amount of dissipated energy in particle–particle interactions.

Also, Zhong et. al. [30, 31] studied the maximum spoutable bed heights of a spout-fluid bed packed with six kinds of Geldart group D particles were. They obtained the effects of particle size, spout nozzle size and fluidizing gas flow rate on the maximum spoutable bed height. Their results shown that the maximum spoutable bed height of spout-fluid bed decreases with increasing particle size and spout nozzle size, which appears the same trend to that of spouted beds. The increasing of fluidizing gas flow rate leads to a sharply decrease in the maximum spoutable bed height. CFD simulation of fluidized bed reactor has also been conducted by Fan et al. [43] focusing on the chemical kinetic aspects and taking into account the intra-particle heat and mass transfer rates, poly-disperse particle distributions and multiphase fluid dynamics. Gas–solid heat and mass transfer, polymerization chemistry and population balance equations were developed and solved in a multi-fluid code (MFIX) in order to describe particle growth. Lettieri et al. [44] used the Eulerian–Eulerian granular kinetic model available within the CFX-4 code to simulate the transition from bubbling to slugging fluidization for a typical Group B material at four fluidizing velocities. Results from simulations were analyzed in terms of voidage profiles and bubble size, which showed typical features of a slugging bed, and also good agreement between the simulated and predicted transition velocity.

In this study, the heat transfer and hydrodynamics of a two-dimensional non-reactive gas–solid fluidized bed reactor were studied experimentally and computationally. Particle size effects, superficial gas velocity and initial static bed height on hydrodynamics of a non-reactive gas–solid fluidized bed reactor were studied experimentally and computationally. Attention was given to the influence of gas temperature and gas velocity on gas-solid heat transfer and hydrodynamics. A multi-fluid Eulerian model incorporating the kinetic theory for solid particles with the standard $k-\varepsilon$ turbulence model was applied in order to simulate the gas–solid flow at different superficial gas velocities. It was assumed that inlet gas was hot and the initial solid particle was at ambient temperature. Simulation results were compared with the experimental data for model validation. The sensitivity of the simulation results to the use of the drag laws of Syamlal-O'Brien, Gidaspow and Cao-Ahmadi was also studied.

2. Governing equations

2.1 Basic equation

The governing equations of the gas-solid flow include the conservation of mass, momentum, and energy. The governing equations of solid and gas phases are based on the Eularian-Eularian model. By definition, the volume fractions of the phases must sum to one:

$$\alpha_g + \alpha_s = 1 \tag{1}$$

The continuity equation for gas and solid phases in the absence of inter-phase mass transfer are respectively given as

$$\frac{\partial}{\partial t}(\alpha_g \rho_g) + \nabla \cdot (\alpha_g \rho_g \overrightarrow{v_g}) = 0 \tag{2}$$

$$\frac{\partial}{\partial t}(\alpha_s \rho_s) + \nabla \cdot (\alpha_s \rho_s \overrightarrow{v_s}) = 0 \tag{3}$$

The conservation of momentum for the gas and solid phases are described by

$$\frac{\partial}{\partial t}(\alpha_g \rho_g \vec{v}_g) + \nabla.(\alpha_g \rho_g \vec{v}_g \vec{v}_g) = -\alpha_g \nabla p_g + \nabla.\overline{\overline{\tau}}_g + \alpha_g \rho_g \vec{g} + \beta_{gs}(\vec{v}_s - \vec{v}_g) \tag{4}$$

$$\frac{\partial}{\partial t}(\alpha_s \rho_s \vec{v}_s) + \nabla \cdot (\alpha_s \rho_s \vec{v}_s \vec{v}_s) = -\alpha_s \nabla p_g - \nabla p_s + \nabla.\overline{\overline{\tau}}_s + \alpha_s \rho_s \vec{g} + \beta_{gs}(\vec{v}_g - \vec{v}_s) \tag{5}$$

Here $\overline{\overline{\tau}}$ is Reynolds stress tensor, g is gravitational constant and $(-\alpha_s \nabla p + \beta_{gs}(\vec{v}_g - \vec{v}_s))$ is an interaction force (drag and buoyancy forces) representing the momentum transfer between gas and solid phases [1, 5, 6]. Several drag models for the gas-solid inter-phase exchange coefficient β_{gs} were reported in the literature. The drag model of Syamlal-O'Brien [20,21], Gidaspow [1] and Cao- Ahmadi [22, 23] were used in the present study. The drag model of Syamlal-O'Brien is based on the measurements of the terminal velocities of particles in fluidized or settling beds. The corresponding inter-phase exchange coefficient is expressed as

$$\beta_{gs} = \frac{3}{4}\frac{\alpha_s \alpha_g \rho_g}{\upsilon_{r,s}^2 d_s} C_D\left(\frac{\mathrm{Re}_s}{\upsilon_{r,s}}\right)\left|\vec{\upsilon}_s - \vec{\upsilon}_g\right| \tag{6}$$

where C_D, the drag coefficient, is given by

$$C_D = \left(0.63 + \frac{4.8}{\sqrt{\mathrm{Re}_s / \nu_{r,s}}}\right)^2 \tag{7}$$

and $\upsilon_{r,s}$, a terminal velocity correlation, is expressed as

$$\upsilon_{r,s} = 0.5\left(A - 0.06\,\mathrm{Re}_s + \sqrt{(0.06\,\mathrm{Re}_s)^2 + 0.12\,\mathrm{Re}_s(2B - A) + A^2}\right) \tag{8}$$

$A = \alpha_g^{4.14}$ and $B = 0.8\alpha_g^{1.28}$ for $\varepsilon_g \le 0.85$ and $B = \alpha_g^{2.65}$ for $\alpha_g > 0.85$

The drag model of Gidaspow is a combination of the Wen and Yu model for dilute flow and the Ergun equation for dense flow. For $\alpha_g < 0.8$, β_{gs} is calculated with the equations from the Wen and Yu [24, 1, 5,8] model as

$$\beta_{gs,Wen-Yu} = \frac{3}{4} C_D \frac{\alpha_g \alpha_s \rho_g \left|\vec{v}_s - \vec{v}_g\right|}{d_s} \alpha_g^{-2.65} \tag{9}$$

where *C*D, the drag coefficient, is expressed as

$$C_D = \frac{24}{\mathrm{Re}_s}\left[1 + 0.15\mathrm{Re}_s^{0.687}\right] \text{ for } \mathrm{Re}_s \geq 1000 \text{ and } C_D = 0.44 \text{ for } \quad \mathrm{Re}_s > 1000 \tag{10}$$

For $\alpha_g \geq 0.8$, β_{gs} is calculated with the Ergun equation as

$$\beta_{gs,Ergun} = 150\frac{\alpha_s^2 \mu_g}{\alpha_g d_s^2} + 1.75\frac{\rho_g \alpha_s \left|\vec{v}_g - \vec{v}_s\right|}{d_s} \tag{11}$$

Cao- Ahmadi drag expression is given as

$$\beta_{gs} = \frac{18\mu_g \alpha_s}{d_s^2} \frac{[1 + 0.1(\mathrm{Re}_s)^{0.75}]}{\left(1 - (\frac{\alpha_s}{\alpha_{s,\max}})\right)^{2.5\alpha_{s,\max}}} \tag{12}$$

where solids Reynolds number, Re_s, is calculated as

$$\mathrm{Re}_s = \frac{\rho_g d_s \left|\vec{v}_g - \vec{v}_s\right|}{\mu_g} \tag{13}$$

Following Gidaspow, it is assumed that the gas and solid phases behave as Newtonian fluids. The constitutive equation for the solid phase stresses is assumed to be given as (Gidaspow, Cao and Ahmadi)

$$\overline{\overline{\tau}}_s = \alpha_s \mu_s \left[\nabla \vec{v}_s + (\nabla \vec{v}_s)^T\right] + \alpha_s \left(\lambda_s - \frac{2}{3}\mu_s\right) \nabla \vec{v}_s \overline{\overline{I}} \tag{14}$$

The granular temperature (Θ) of the solid phase is defined as one-third of the mean square particle velocity fluctuations. It should be emphasized that the granular temperature is proportional to the granular energy and is quite different from solid phase thermodynamic temperature. The transport equation for the solid phase granular temperature is given as [27, 29, 30].

$$\frac{3}{2}\frac{\partial}{\partial t}(\rho_s \alpha_s \Theta_s) + \nabla \cdot (\rho_s \alpha_s \vec{v}_s \Theta_s) = (-p_s \overline{\overline{I}} + \overline{\overline{\tau}}_s) : \nabla \cdot \vec{v}_s + \nabla \cdot (k_{\Theta_s} \nabla \Theta_s) - \gamma_{\Theta_s} + \phi_{gs} \tag{15}$$

where $(-p_s \overline{\overline{I}} + \overline{\overline{\tau}}_s) : \nabla . \vec{v}_s$ is the generation of energy by the solid stress tensor, $k_{\Theta_s} \nabla \Theta_s$ is the diffusion flux of granular energy (k_{Θ_s} is the diffusion coefficient), γ_{Θ_s} is the collisional dissipation of energy and φ_{gs} is the energy exchange between the gas and solid. The collision dissipation of energy, γ_{Θ_s}, representing the rate of energy dissipation within the solid phase due to inelastic particle collisions that was derived by Lun et al. [29] is given as

$$\gamma_{\Theta_s} = \frac{12(1-e_{ss}^2)g_{o,ss}}{d_s\sqrt{\pi}}\rho_s\alpha_s^2\Theta_s^{3/2} \tag{16}$$

The transfer of kinetic energy, φ_{gs}, due to random fluctuations in particle velocity is expressed as [1]

$$\varphi_{gs} = -3\beta_{gs}\Theta_s \tag{17}$$

A complete solution procedure of the above equation has not yet been developed. Jenkins and Mancini [30] have developed a theoretical description of a suspension with more than one particle size, employing the kinetic theory of granular flow. They predicted transport properties of binary mixture assuming equal granular temperature [9-11]. Gidaspow et al. [1, 11] have extended the kinetic theory of dense gases for binary granular mixture with unequal granular temperature between the particle phases. In the some researches [10, 14-16] the following algebraic granular temperature equation was used with the assumptions that the granular energy is dissipated locally, the convection and diffusion contributions are negligible and retaining only the generation and dissipation terms. Also van Wachem et al. [14-16] have shown that this assumption is feasible in the bubbling region of a fluidized bed. When using this algebraic equation in stead of solving the balance for the granular temperature, much faster convergence is obtained during simulations.

$$\Theta_s = \left\{ \frac{-K_1\alpha_s tr\left(\overline{\overline{D}}_s\right) + \sqrt{K_1{}^2 tr^2\left(\overline{\overline{D}}_s\right)\alpha_s^2 + 4K_4\alpha_s\left[K_2 tr^2\left(\overline{\overline{D}}_s\right) + 2K_s tr\left(\overline{\overline{D}}_s{}^2\right)\right]}}{2\alpha_s K_4} \right\}^2 \tag{18}$$

where $\overline{\overline{D}}_s$ is the solids strain rate tensor, and with the abbreviations :

$$\overline{\overline{D}}_s = \frac{1}{2}\left[\nabla\vec{v}_s + (\nabla\vec{v}_s)^T\right] \tag{19}$$

$$K_1 = 2(1+e_{ss})\rho_s g_{0,ss} \tag{20}$$

$$K_2 = \frac{4}{3\sqrt{\pi}}d_s\rho_s(1+e_{ss})\alpha_s g_{0,ss} - \frac{2}{3}K_3 \tag{21}$$

$$K_3 = \frac{d_s\rho_s}{2}\left\{\frac{\sqrt{\pi}}{3(3-e_{ss})}\left[1+0.4(1+e_{ss})(3e_{ss}-1)\alpha_s g_{0,ss}\right] + \frac{8\alpha_s g_{0,ss}(1+e_{ss})}{5\sqrt{\pi}}\right\} \tag{22}$$

$$K_4 = \frac{12(1-e_{ss}^2)\rho_s g_{0,ss}}{d_s\sqrt{\pi}} \tag{23}$$

For granular flows a solids pressure is calculated independently and used for the pressure gradient term, p_s, in the granular-phase momentum equation. Because a Maxwellian

velocity distribution is used for the particles, a granular temperature is introduced into the model and appears in the expression for the solid pressure and viscosities. The solid pressure is composed of a kinetic term and a second term due to particle collisions:

$$p_s = \alpha_s \rho_s \Theta_s + 2\rho_s (1+e_{ss}) \alpha_s^2 g_{o,ss} \Theta_s \tag{24}$$

where e_{ss} is the coefficient of restitution for particle collisions. This coefficient is a measure of the elasticity of the collision between two particles, and relates to how much of the kinetic energy of the colliding particles before the collision remains after the collision. A perfectly elastic collision has a coefficient of restitution of 1. A perfectly plastic, or inelastic, collision has a coefficient of restitution of 0 [8, 9]. The coefficient of restitution is defined as the ratio of the difference in the velocities of the two colliding particles after the collision to that in their velocities before the collision, i.e.,

$$e_{ss} = \frac{\text{Speed of separation}}{\text{Speed of approaching}} \tag{25}$$

e_{ss} can be derived from Newton's equation of motion. It is a function of the material properties, impact velocity and hardness ratio. But, under near-elastic conditions the coefficient of restitution of a particle is approximately constant, and the assumption of a constant e_{ss} could greatly simplify mathematical manipulation of CFD simulation [8,9]. $g_{o,ss}$ is the radial distribution function that for one solids phase, use

$$g_{o,ss} = \left[1 - \left(\frac{\alpha_s}{\alpha_{s,\max}} \right)^{\frac{1}{3}} \right]^{-1} \tag{26}$$

At a packed state, the bed is crammed with particles, and hence the frictional force prevails over the other forces, while at a fluidized state, lasting contact gives way to free flight and brief collisions among particles. The competition and transformation of dominating forces lead to flow transition from the packed bed to fluidization. Subsequently, three mechanisms of the particle-phase transport result in two types of flow states, as shown in Fig. 2. The frictional transport determines the behaviors at a close packed state, while the kinetic collisional transports cause a two-phase flow. So, the total stress may be approximated as the sum of frictional and kinetic collisional contributions as if each of them acts alone. so, the solids stress tensor contains shear and bulk viscosities arising from particle momentum exchange due to translation and collision.

The solid stress tensor contains shear and bulk viscosities arising from particle momentum exchange due to translation and collision. A frictional component of viscosity can also be included to account for the viscous-plastic transition that occurs when particles of a solid phase reach the maximum solid volume fraction.

The collisional and kinetic parts, and the frictional part, were used to evaluate the solid shear viscosity. That is,

$$\mu_s = \mu_{s,col} + \mu_{s,kin} + \mu_{s,fr} \tag{27}$$

The collisional part of the shear viscosity is modeled as

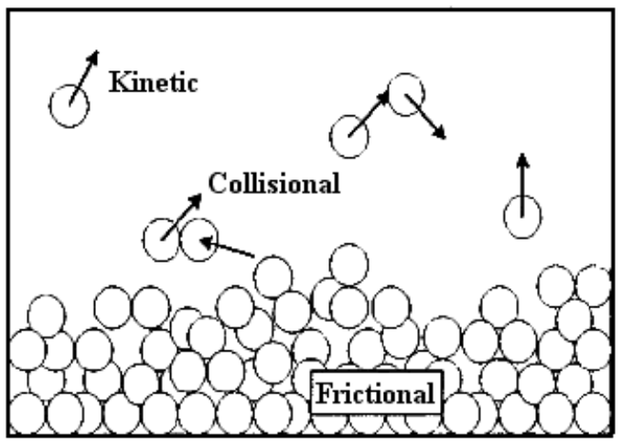

Fig. 2. Three particle transport mechanisms: kinetic, collisional, and frictional transport.

$$\mu_{s,col} = \frac{4}{5}\alpha_s \rho_s d_s g_{o,ss}(1+e_{ss})\left(\frac{\Theta_s}{\pi}\right)^{1/2} \tag{28}$$

The kinetic term is expressed in the Syamlal-O'Brien [20, 21] model as :

$$\mu_{s,kin} = \frac{\alpha_s \rho_s d_s \sqrt{\Theta_s \pi}}{6(3-e_{ss})}\left[1+\frac{2}{5}(1+e_{ss})(3e_{ss}-1)\alpha_s g_{o,ss}\right] \tag{29}$$

Gidaspow et al. suggested:

$$\mu_{s,kin} = \frac{10\rho_s d_s \sqrt{\Theta_s \pi}}{96(1+e_{ss})g_{o,ss}}\left[1+\frac{4}{5}g_{o,ss}\alpha_s(1+e_{ss})\right]^2 \tag{30}$$

Also Cao and Ahmadi [22, 23] suggested:

$$\begin{aligned}\mu_s = &\left[1+\left(\tau_g^t/\tau_{gs}^x\right)\left(1-\alpha_s/\alpha_{s,\max}\right)^3\right]^{-1} \times \\ &\left[0.1045\left(1/g_{0,ss}+3.2\alpha_s+12.1824 g_{0,ss}\alpha_s^2\right)\right] d_s \rho_s \sqrt{\Theta_s}\end{aligned} \tag{31}$$

where the particle relaxation time, τ_{gs}^x , and time-scale of turbulent eddies, τ_g^t , are given by

$$\tau_{gs}^x = \frac{\alpha_s \rho_s}{\beta_{gs}}, \quad \tau_g^t = \frac{3}{2}C_\mu \frac{k_g}{\varepsilon_g} \tag{32}$$

Here k_g is the turbulent kinetic energy of gas phase, C_μ is the constant in the gas turbulence model, and ε_g is the turbulent energy dissipation in the gas phase.
The friction stress plays a significant role when the solid-phase volume fraction gets close to the packing limit. For the contribution of the friction stress to the solid shear viscosity the expression suggested by Schaeffer [8] given as

$$\mu_{s,fr} = \frac{p_s \sin\varphi}{2\sqrt{I_{2D}}} \tag{33}$$

$$I_{2D} = \frac{1}{6}\left[\left(D_{s11} - D_{s22}\right)^2 + \left(D_{s22}\right)^2 + \left(D_{s11}\right)^2\right] + D_{s12}^2 \tag{34}$$

$$I_{2D} = \frac{1}{6}\left[\left(\frac{\partial u_s}{\partial x} - \frac{\partial v_s}{\partial y}\right) + \left(\frac{\partial v_s}{\partial y}\right)^2 + \left(\frac{\partial u_s}{\partial x}\right)^2\right] + \left[\frac{1}{2}\left(\frac{\partial u_s}{\partial y} + \frac{\partial v_s}{\partial x}\right)\right]^2 \tag{35}$$

is used. Here p_s is the solid pressure, φ is the angle of internal friction, and I_{2D} is the second invariant of the deviatoric stress tensor [5, 8, 11]. The solid bulk viscosity accounts for the resistance of the granular particles to compression and expansion. It has the following from Lun et al. [29]:

$$\lambda_s = \frac{4}{3}\alpha_s \rho_s d_s g_{o,ss}(1+e_{ss})\sqrt{\frac{\Theta_s}{\pi}} \tag{36}$$

Also Cao and Ahmadi [22,23] suggested

$$\lambda_s = \frac{5}{3}\left[1 + \left(\tau_1^t/\tau_{12}^x\right)\left(1-\alpha_s/\alpha_{s,\max}\right)^3\right]^{-1}\left[0.1045\left(12.1824 g_{0,ss}\alpha_s^2\right)\right] d_s \rho_s \sqrt{\Theta_s} \tag{37}$$

The diffusion coefficient for granular energy, k_{Θ_s} , is expressed by two different models. The Syamlal- O'Brien model expresses as [20, 21]

$$k_{\Theta_s} = \frac{15 d_s \rho_s \alpha_s \sqrt{\pi\Theta_s}}{4(41-33\eta)}\left[1 + \frac{12}{5}\eta^2(4\eta-3)\alpha_s g_{o,ss} + \frac{16}{15\pi}(41-33\eta)\eta\alpha_s g_{o,ss}\right] \tag{38}$$

With $\eta = \frac{1}{2}(1+e_{ss})$

and the Gidaspow model express k_{Θ_s} as [1]

$$k_{\Theta_s} = \frac{150\rho_s d_s\sqrt{\Theta_s \pi}}{384(1+e_{ss})g_{o,ss}}\left[1 + \frac{6}{5}g_{o,ss}\alpha_s(1+e_{ss})\right]^2 + 2\alpha_s^2\rho_s d_s g_{o,ss}(1+e_{ss})\left(\frac{\Theta_s}{\pi}\right)^{1/2} \tag{39}$$

The minimum fluidization velocity is calculated from Ergun equation for spherical particles.

$$\frac{1.75}{\alpha_{s,\max}^3}\left(\frac{d_s U_{mf}\rho_g}{\mu_g}\right)^2 + \frac{150(1-\alpha_{mf})}{\alpha_{s,\max}^3}\left(\frac{d_s U_{mf}\rho_g}{\mu_g}\right) = \frac{d_s^3\rho_g(\rho_s-\rho_g)g}{\mu_g^2} \tag{40}$$

From equation (32) and parameters of Table.1, the minimum fluidization velocity (U_{mf}) for three particle sizes, 0.175, 0.275 and 0.375 mm, was calculated as 0.042, 0.065 and 0.078 m/s, respectively.

The internal energy balance for the gas phase can be written in terms of the gas temperature as follows:

$$\alpha_g \rho_g Cp_g \left(\frac{\partial T_g}{\partial t} + v_g . \nabla T_g \right) = -H_{gs} \tag{41}$$

The solid heat conductivity includes direct conduction through the fractional contact area and indirect conduction through a wedge of the gas that is trapped between the particles. Since the gas heat conductivity is negligible, the heat diffusion term has been ignored [11].
The thermal energy balance for the solid phases is given by

$$\alpha_s \rho_s Cp_s \left(\frac{\partial T_s}{\partial t} + v_s . \nabla T_s \right) = \nabla . \alpha_s K_s \nabla T_s + H_{gs} \tag{42}$$

Solid granular conductivity is obtained using the Ahmadi model

$$K_s = 0.1306 \rho_s d_s (1 + e_{ss}{}^2)(\frac{1}{g_{0,ss}} + 4.8\alpha_s + 12.1184 g_{0,ss} \alpha_s^2)\sqrt{\Theta_s} \tag{43}$$

The heat transfer between the gas and the solid is a function of the temperature difference between the gas and solid phases:

$$H_{gs} = -\gamma^0{}_{gs} \left(T_s - T_g \right) \tag{44}$$

The heat transfer coefficient is related to the particle Nusselt number using the following equation:

$$\gamma^0_{gs} = \frac{6 k^{'}_g \alpha_s Nu_s}{d_s^2} \tag{45}$$

Here $k^{'}_g$ is the thermal conductivity of the gas phase. The Nusselt number is determined applying the following correlation

$$\begin{aligned} Nu_s = & \left(7 - 10\alpha_g + 5\alpha_g^2\right)\left(1 + 0.7 \,\mathrm{Re}_s{}^{0.2} \,\mathrm{Pr}^{1/3}\right) + \\ & \left(1.33 - 2.4\alpha_g + 1.2\alpha_g^2\right)\mathrm{Re}_s^{0.7} \,\mathrm{Pr}^{1/3} \end{aligned} \tag{46}$$

2.2 Turbulence model

The standard $k-\varepsilon$ model has become the workhorse of practical engineering flow calculations since it was proposed by Launder and Spalding. Robustness, economy, and reasonable accuracy for a wide range of turbulent flows explain its popularity in industrial flow and heat transfer simulations. The standard $k-\varepsilon$ model is a semi-empirical model based on model transport equations for the turbulence kinetic energy (k) and its dissipation rate (ε). The model transport equation for k is derived from the exact equation, while the model transport equation for ε was obtained using physical reasoning and bears little resemblance to its mathematically exact counterpart [30-34].
The Reynolds stress tensor for the gas phase is

$$\overline{\overline{\tau}}_g = -\frac{2}{3}(\rho_g k_g + \rho_g \mu_{t,g} \nabla . \overrightarrow{v_g})\overline{\overline{I}} + \rho_g \mu_{t,g} \left[\nabla \overrightarrow{v_s} + (\nabla \overrightarrow{v_s})^T \right] \tag{47}$$

Symbol	Description	Value	Comment or reference
ρ_s	Solids density	1830 kg/m^3	Glass beads
ρ_g	Gas density	1.189 kg/m^3	Air at ambient conditions
d_s	Mean particle diameter	(Geldart B type)	Uniform distribution
e_{ss}	Coefficient of restitution	0.9	Fixed value
$\alpha_{\max}$	Maximum solids packing	0.61	Syamlal et al. [20,21]
φ	Angle of internal friction	25	Johnson and Jackson [33]
V_{mf}	Minimum fluidization velocity	5.5 cm/s	from Ergun [1,2]
D_t	Column diameter	25 cm	Fixed value
H_1	Fluidized bed height	100 cm	Fixed value
H_0	Initial static bed height	30, 40 cm	Specified
	Initial temperature of solids	300 K	Fixed value
	Inlet gas temperature	473 K	Fixed value
V_g	Superficial gas velocity	0- 1000 cm/s	A range was used
	Inlet boundary conditions	Velocity	Superficial gas velocity
	Outlet boundary conditions	Out flow	Fully developed flow
Δt	Time steps	0.001 s	Specified
	Maximum number of iterations	20	Specified
	Convergence criteria	10^{-3}	Specified

Table 1. Values of model parameters used in the simulations and experiments.

The turbulence kinetic energy, k, and its rate of dissipation, ε, are obtained from the following transport equations (modified $k-\varepsilon$ model):

$$\frac{\partial}{\partial t}(\alpha_g \rho_g k_g) + \nabla.(\alpha_g \rho_g \overrightarrow{v_g} k_g) = \nabla.(\alpha_g \frac{\mu_{t,g}}{\sigma_k} \nabla k_g) + \alpha_g G_{k,g} - \alpha_g \rho_g \varepsilon_g + \alpha_g \rho_g \prod_{k,g} \tag{48}$$

$$\frac{\partial}{\partial t}(\alpha_g \rho_g \varepsilon_g) + \nabla.(\alpha_g \rho_g \overrightarrow{v_g} \varepsilon_g) = \nabla.(\alpha_g \frac{\mu_{t,g}}{\sigma_\varepsilon} \nabla \varepsilon_g) + \alpha_g \frac{\varepsilon_g}{k_g}(C_{1\varepsilon} C_{k,g} - C_{2\varepsilon} \rho_g \varepsilon_g) + \alpha_g \rho_g \prod_{\varepsilon,g} \tag{49}$$

$\prod_{k,g}$ and $\prod_{\varepsilon,g}$ represent the influence of the dispersed phase on the continuous phase. Predictions of the turbulence quantities of the dispersed phase are obtained using the Tchen theory [7] of dispersion of discrete particles by homogeneous turbulence. In the transport equation for k, $G_{k,g}$ is the production of turbulence kinetic energy and is defined as

$$G_{k,g} = -\rho_g \overline{u_i' u_j'} \frac{\partial u_j}{\partial x_i} \tag{50}$$

The model constants $C_{1\varepsilon}, C_{2\varepsilon}, C_\mu, \sigma_k$, and σ_k have the values
$C_{1\varepsilon} = 1.44 \quad C_{2\varepsilon} = 1.92 \quad C_\mu = 0.09 \quad \sigma_k = 1.0 \quad \sigma_\varepsilon = 1.3$

For granular energy dissipation and turbulence interaction terms, Ahmadi suggested respectively

$$\varepsilon_s = 12(1-e_{ss}^2)\alpha_s^2\rho_s g_{o,ss}\frac{\Theta_s^{3/2}}{d_s} \tag{51}$$

$$\Pi_{k,g} = \beta_{sg}(3\Theta_s - 2k_g)\ ,\ \Pi_{\varepsilon,g} = 0\ ,\ \Pi_{k,s} = \beta_{sg}\left(\frac{2k_g}{1+\tau_{gs}^x/\tau_g} - 3\Theta_s\right) \tag{52}$$

Also, for gas turbulent viscosity, Ahmadi suggested

$$\mu_g^t = \rho_g C_\mu\left[1+\left(\tau_{sg}^x/\tau_g^t\right)\left(\alpha_s/\alpha_{s,\max}\right)^3\right]^{-1}\frac{k_g^2}{\varepsilon_g} \tag{53}$$

2.3 Initial and boundary conditions

The initial values of the variables for all the fields $(\alpha_g, \alpha_s, v_g, v_s)$ are specified for the entire computational domain. Initially, solid particle velocity was set at zero (in minimum fluidization), and gas velocity was assumed to have the same value everywhere in the bed. At the inlet, all velocities and volume fraction of all phases were specified. Outlet boundary condition was out flow and was assumed to be a fully developed flow. The other variables were subject to the Newmann boundary condition. The gas tangential normal velocities on the wall were set to zero (no slip condition). The normal velocity of the particles was also set at zero. The following boundary condition was applied for the tangential velocity of particles at the wall [28-35]

$$\vec{v}_{s,w} = -\frac{6\mu_s\alpha_{s,\max}}{\sqrt{3}\pi\rho_s\alpha_s g_{o,ss}\sqrt{\Theta_s}}\frac{\partial\vec{v}_{s,w}}{\partial n}. \tag{54}$$

The general boundary condition for granular temperature at the wall takes the form

$$\Theta_{s,w} = -\frac{k_s\Theta_s}{e_{ss,w}}\frac{\partial\Theta_{s,w}}{\partial n} + \frac{\sqrt{3}\pi\rho_s\alpha_s v_s^2 g_o\Theta_s^{3/2}}{6\alpha_{s,\max}e_{ss,w}} \tag{55}$$

Here $\vec{v}_{s,w}$ is the particle slip velocity, $e_{ss,w}$ is the restitution coefficient at the wall, and $\alpha_{s,\max}$ is the volume fraction for the particles at maximum packing. The boundary conditions for the energy equation are set such that the walls are adiabatic. Initial solid particles temperature is 300K and the inlet gas temperature is 473K.

3. Model solution procedure

Two-dimensional (2D) simulations of the fluidized bed with heat transfer under steady conditions were performed and the results are described in this section. The Eulerian multiphase model described earlier was used for the analysis. The 2D computational domain was discretized using 8600 rectangular cells. Typically, a time step of 0.001s with 20

iterations per time step was also used. This number of iterations was found to be adequate to achieve convergence for the majority of time steps. Table 1 shows values of model parameters that were used in the simulations.

The discretized governing equations were solved by the finite volume method employing the Semi Implicit Method for the Pressure Linked Equations (SIMPLE) algorithm that was developed by Patankar and Spalding for multiphase flow using the Partial Elimination Algorithm (PEA). Several research groups have used extensions of the SIMPLE method, which appears to be the method of choice in commercial CFD codes. Two modifications of the standard extensions of SIMPLE have been introduced in the present simulations to improve the stability and speed of computations. i) A solid volume fraction correction equation (instead of a solid pressure correction equation) was used. This appears to help the convergence when the solids are loosely packed. That equation also incorporates the effect of solid pressure that helps to stabilize the calculations in densely packed regions. ii) The automatic time-step adjustment was used to ensure that the run progresses with the highest execution speed. In this paper an approximate calculation of the normal velocity at the interfaces (defined by a small threshold value for the phase volume fraction) was used. Gas-solid flows are inherently unstable. For vast majority of gas-solid flows, a transient simulation analysis was conducted and the results were time-averaged. Transient simulations diverge if a large time-step is used. Using a very small time step makes the computations very slow. Therefore, the time step was automatically adjusted to reduce the computational time [39, 40].

The first order upwind scheme was used for discretization of the governing equations. The computational domain was divided into a finite number of control volumes. Volume fraction, density and turbulent kinetic energy were stored at the main grid points that were placed in the center of each control volume. A staggered grid arrangement was used, and the velocity components were solved at the control volume surfaces. The conservation equations were integrated in the space and time. The sets of resulting algebraic equations were solved iteratively [38-43].

The following steps were followed in the simulations:

1. Initially the physical properties and exchange coefficients are calculated.
2. Velocity fields based on the current pressure field and the corresponding u_m^*, v_m^* (m = 0, 1 for solid and gas phases) are evaluated.
3. The fluid pressure correction P_g' is calculated.
4. The fluid pressure field is updated applying an under-relaxation, $P_g = P_g^* + \omega_{sg} P_g'$.
5. The fluid velocity corrections from P_g' are evaluated, and the fluid velocity fields are updated using, $u_m = u_m^* + u_m'$.
   (Similarly the solid phase velocities u_s as denoted in step 9 are updated).
6. The pressure gradients, $\frac{\partial P_m}{\partial \alpha_m}$, are evaluated for use in the solid volume fraction correction equation.
7. The solid volume fraction correction α_m' is evaluated.
8. The solid volume fraction is updated. That is, $\alpha_m' = \alpha_m^* + \omega_{gs} \alpha_m'$.
9. The velocity corrections for the solid phase are estimated and the solid velocity fields are updated. That is, $u_s = u_s^* + u_s'$.

10. The solid pressure is evaluated.
11. The temperatures and the turbulence property are evaluated.

The normalized residuals calculated in Steps 2, 3, 5, and 9 are used to check for convergence [37, 39, 40, 41]. If the convergence criterion is not satisfied, then the iterations starting with Step 2 are repeated. The flowchart of the simulation algorithm for one time step is shown in Fig. 3.

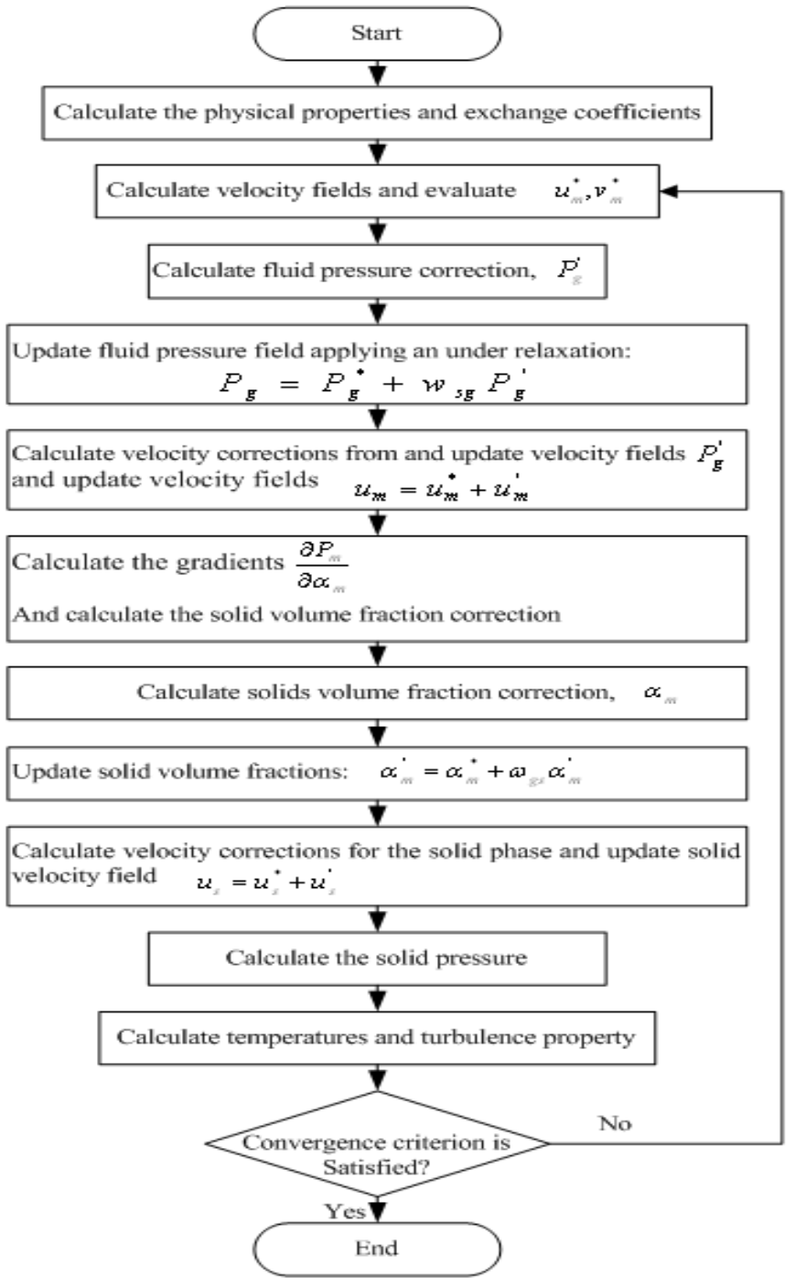

Fig. 3. Flowchart of the simulation procedure for one time step.

Sensitivity analysis of the effect of the time step, discretization schemes, and convergence criterion on the results was also studied. The simulated results for the solid volume fraction profile from the first-order discretization schemes for a time step of 0.001s with 10^{-3} convergence criterion (the typical numerical procedure for this study) were compared with those of first and second-order discretization schemes, for a time step of 0.0005s, and 10^{-4} convergence criterion with 50 iterations at each time step. (These high quality numerical procedures require additional computational time.) The simulation results show no noticeable difference in overall hydrodynamic behavior, temperature distribution and bubble shapes among these simulations; therefore, it is concluded that the selected numerical parameters are adequate for proper simulations of bed hydrodynamic with heat transfer.

4. Experimental setup

A bench scale experimental setup for studying gas-solid flows and heat transfer was designed and fabricated. The setup consists of a Pyrex cylinder with a height of 100cm and a diameter of 25 cm as shown schematically in Fig. 4. The air was injected through a

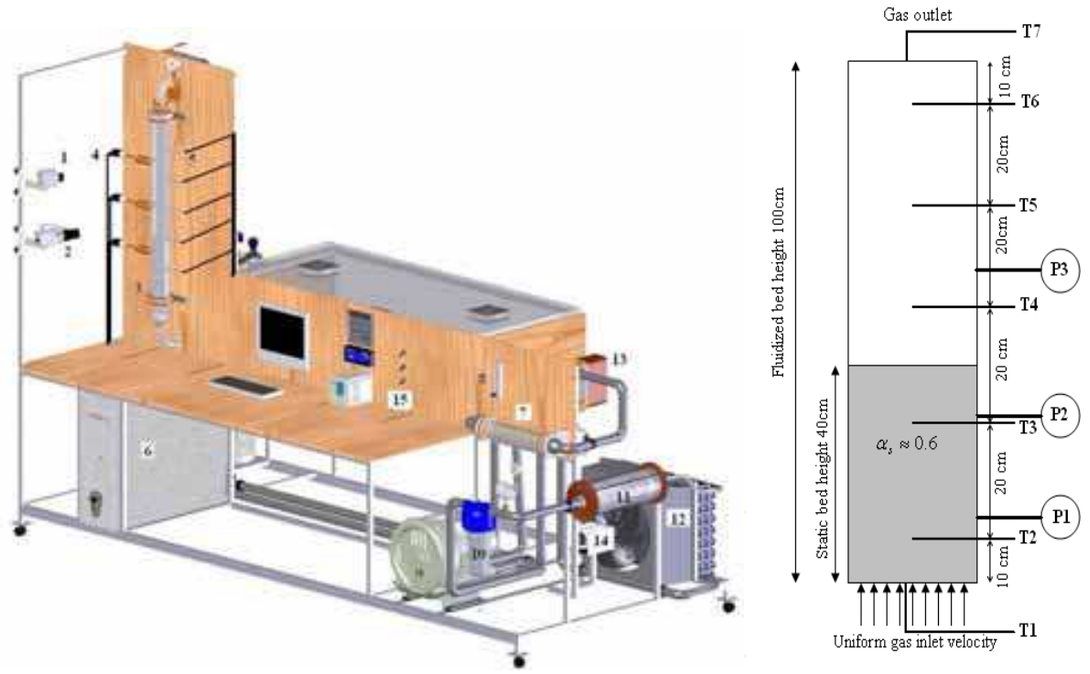

(A) (B)

Fig. 4. (A): A view of experimental set-up (1- digital camera, 2- digital video recorder, 3- Pyrex reactor, 4- pressure transducers, 5-thermocouples, 6- computer , A/D and DVR cards, 7- electrical heater, 8-rotameter, 9-blower, 10- filter, 11-14- cooling system, 15- controller system), (B) : pressure transducer and thermocouple positions in the fluidized bed reactor

perforated plate with an open area of 0.8 % and an orifice diameter of 2 cm. Under this plate there was a homogenization system to prevent the gas flow from generating asymmetrical effects inside the free board. This distribution belongs to group B in the Geldart

classification. Spherical particles with different diameter and a density of 1830 kg/m^3 were fluidized with air at ambient conditions. Typically, the static bed height was 30 and 40cm with a solid volume fraction of 0.6. A roots-type blower supplied the fluidizing gas. A pressure-reducing valve was installed to avoid pressure oscillations and achieve a steady gas flow. The airflow rate was measured using a gas flow meter (rotameter) placed between the blower and the inlet pipe to an electrical heater. Initial solid particle temperature was 300K. An electrical heater was used to increase the inlet gas temperature from ambient temperature to 473K. A cooling system was used to decrease the gas temperature that exited from the reactor in order to form a closed cycle. Fig. 4 (A) shows a schematic of experimental set-up and its equipments.

Pressure fluctuations in the bed were measured by three pressure transducers. The pressure transducers were installed in the fluidized bed column at different heights. Seven thermocouples (Type J) were installed in the center of the reactor to measure the variation of gas temperature at different locations. Also, three thermocouples were used in different positions in the set-up to control the gas temperature in the heat exchanger and cooling system. Fig. 4. (B) shows the locations of the pressure transducers and thermocouples. The pressure probes were used to convert fluctuation pressure signals to out-put voltage values proportional to the pressure. The output signal was amplified, digitized, and further processed on-line using a Dynamic Signal Analyzer. Analog signals from the pressure transducers were band pass filtered (0–25 Hz) to remove dc bias, prevent aliasing, and to remove 50 Hz noise associated with nearby ac equipment. The ratio of the distributor pressure drop to the bed pressure drop exceeded 11% for all operating conditions investigated. The overall pressure drop and bed expansion were monitored at different superficial gas velocities from 0 to 1 m/s.

For controlling and monitoring the fluidized bed operation process, A/D, DVR cards and other electronic controllers were applied. A video camera (25 frames per s) and a digital camera (Canon 5000) were used to photograph the flow regimes and bubble formation through the transparent wall (external photographs) during the experiments. The captured images were analyzed using image processing software. The viewing area was adjusted for each operating condition to observe the flow pattern in vertical cross sections (notably the bed height oscillations). Image processing was carried out on a power PC computer equipped with a CA image board and modular system software. Using this system, each image had a resolution of 340×270 pixels and 256 levels of gray scales. After a series of preprocessing procedures (e.g., filtering, smoothing, and digitization), the shape of the bed, voidage, and gas volume fraction were identified. Also, the binary system adjusted the pixels under the bed surface to 1 and those above the bed surface to 0. The area below the bed surface was thus calculated, and then divided by the side width of the column to determine the height of the bed and the mean gas and solid volume fraction.

Some of experiments were conducted in a Plexiyglas cylinder with 40cm height and 12 cm diameter (Fig. 5). At the lower end of this is a distribution chamber and air distributor which supports the bed when defluidized. This distributor has been designed to ensure uniform air flow into the bed without causing excessive pressure drop and is suitable for the granular material supplied. A Roots-type blower supplied the fluidizing gas. A pressure-reducing valve was installed to avoid pressure oscillations and to achieve a steady gas flow. Upon leaving the bed, the air passes through the chamber and escapes to the atmosphere through a filter. Installed in the bracket are probes for temperature and pressure

measurement, and a horizontal cylindrical heating element, all of which may move vertically to any level in the bed chamber.

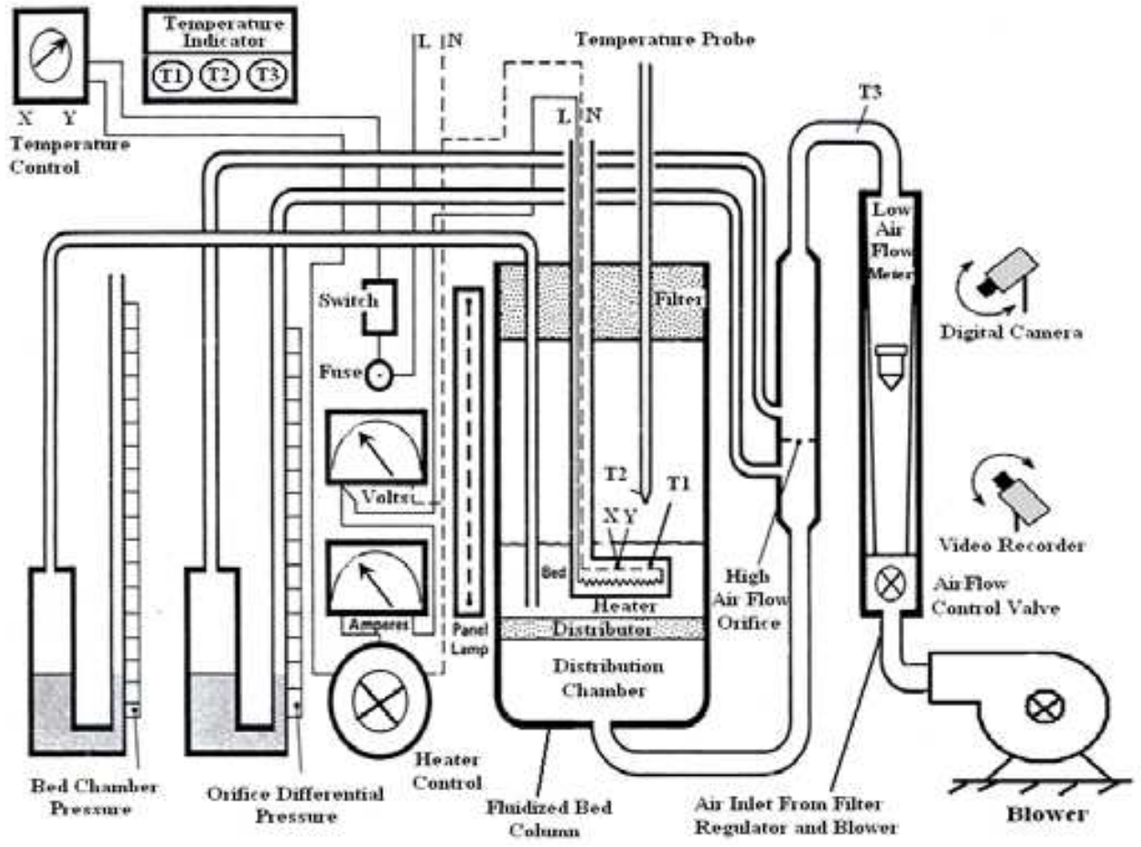

Fig. 5. A view of experimental set-up with its equipments.

Air is delivered through a filter, pressure regulator and an air flow meter fitted with a control valve and an orifice plate (to measure higher flow rates), to the distribution chamber. The heat transfer rate from the heating element is controlled by a variable transformer, and the voltage and current taken are displayed on the panel. Two thermocouples are embedded in the surface of the element. One of these indicates the surface temperature and the other, in conjunction with a controller, prevents the element temperature exceeding a set value. A digital temperature indicator with a selector displays the temperatures of the element, the air supply to the distributor, and the moveable probe in the bed chamber. Two liquid filled manometers are fitted. One displays the pressure of the air at any level in the bed chamber, and the other displays the orifice differential pressure, from which the higher air flow rates can be determined. Pressure fluctuations in the bed are obtained by two pressure transducers that are installed at the lower and upper level of the column. The electrical heater increases the solid particle temperature, so, initial solid particles temperature was 340K and for inlet air was 300K (atmospheric condition). The ratio of the distributor pressure drop to the bed pressure drop exceeded 14% for all operating conditions investigated.

5. Results and discussion

Simulation results were compared with the experimental data in order to validate the model. Pressure drop, Δp, bed expansion ratio, H/H_0, and voidage were measured experimentally for different superficial gas velocities; and the results were compared with those predicted by the CFD simulations. Fig. 6 compares the predicted bed pressure drop using different drag laws with the experimentally measured values.

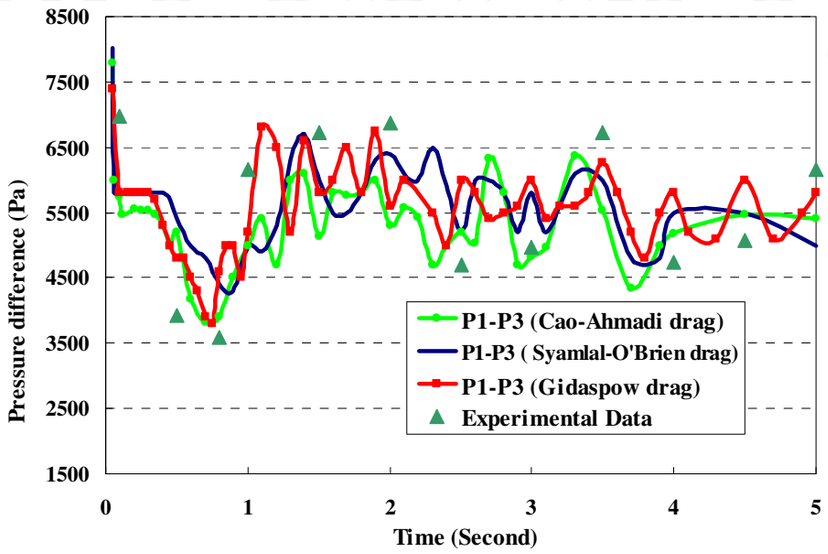

Fig. 6. Comparison of simulated bed pressure drop using different drag models with the experimental data for a superficial velocity of V_g = 50 cm/s.

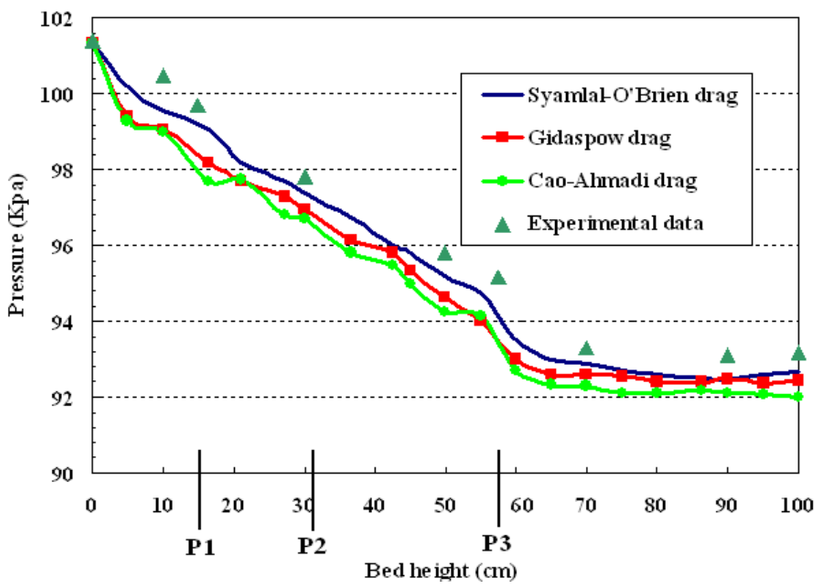

Fig. 7. Comparison of simulated pressure variation versus bed height using Cao-Ahmadi, Syamlal–O'Brien and Gidaspow drag models with the experimental data for a superficial velocity of V_g = 50 cm/s and position of pressure transducers (P1, P2 and P3).

Fig. 7 compares the simulated pressure variations versus the bed height for different drag laws with the experimentally measured values. The positions of pressure transducers (P1, P2 and P3) that were shown in Fig. 4(B) are identified in this Fig. To increase the number of experimental data for the pressure in the bed, five additional pressure transducers were installed at the thermocouple locations, and the corresponding pressures for a superficial velocity of V_g = 50 cm/s were measured. The air enters into the bed at atmospheric pressure and decreases roughly linearly from bottom up to a height of about 60 cm due to the presence of a high concentration of particles. At the bottom of the bed, the solid volume fraction (bed density) is large; therefore, the rate of pressure drop is larger. Beyond the height of 60cm (up to 100cm), there are essentially no solid particles, and the pressure is roughly constant. All three drag models considered show comparable decreasing pressure trends in the column. The predictions of these models are also in good agreement with the experimental measurements. Fig.s 6 and 7 indicate that there is no significant difference between the predicted pressure drops for different drag models for a superficial gas velocity of V_g = 50 cm/s.

Figs. 6 and 7 show that there is no significant difference between the predicted pressure drops and bed expansion ratio for the different drag models used. That is the fluidization behavior of relatively large Geldart B particles for the bed under study is reasonably well predicted, and all three drag models are suitable for predicting the hydrodynamics of gas–solid flows.

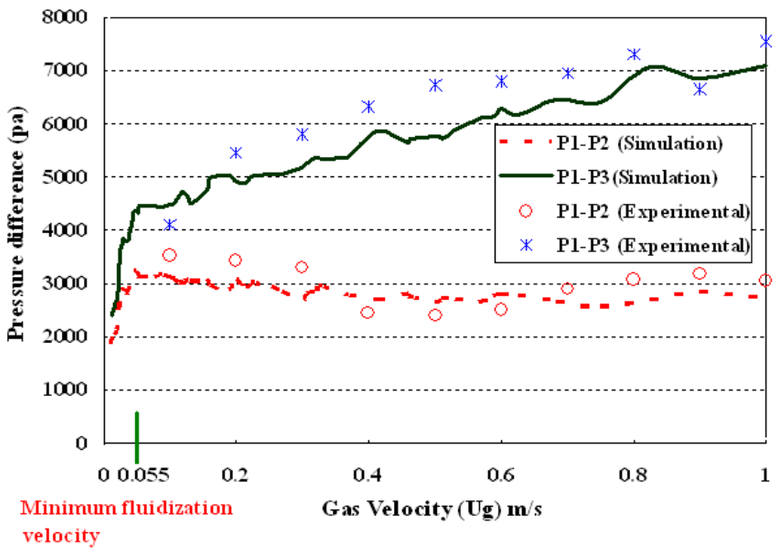

Fig. 8. Comparison of experimental and simulated bed pressure drop versus superficial gas velocity.

Fig. 8 compares the simulated time-averaged bed pressure drops, (P1-P2) and (P1-P3), against the superficial gas velocity with the experimental data. The Syamlal–O'Brien drag expression was used in these simulations. The locations of pressure transducers (P1, P2, P3) were shown in Fig. 4 (B). The simulation and experimental results show good agreement at velocities above $V_{mf.}$. For $V < V_{mf,}$ the solid is not fluidized, and the bed dynamic is dominated by inter-particle frictional forces, which is not considered by the multi-fluid models used. Fig. 8 shows that with increasing gas velocity, initially the pressure drops

(P1-P2 and P1-P3) increase, but the rate of increase for (P1-P3) is larger than that for (P1-P2). For $V > V_{mf}$ this Fig. shows that (P1-P3) increases with gas velocity, while (P1-P2) decreases slightly, stays roughly constant, and increases slightly. This trend is perhaps due to the expansion of the bed and the decrease in the amount of solids between ports 1 and 2. As the gas velocity increases further, the wall shear stress increases and the pressure drop begins to increase. Ports 1 and 3 cover the entire height of the dense bed in the column, and thus (P1-P3) increases with gas velocity.

As indicated in Fig. 9, the bed overall pressure drop decreased significantly at the beginning of fluidization and then fluctuated around a near steady-state value after about 3.5 s. Pressure drop fluctuations are expected as bubbles continuously split and coalesce in a transient manner in the fluidized bed. The results show with increasing the particles size, pressure drop increase. Comparison of the model predictions, using the Syamlal–O'Brien drag functions, and experimental measurements on pressure drop show good agreement for most operating conditions. These results (for d_s=0.275 mm) are the same with Tagipour et al. [8] and Behjat et al. [11] results.

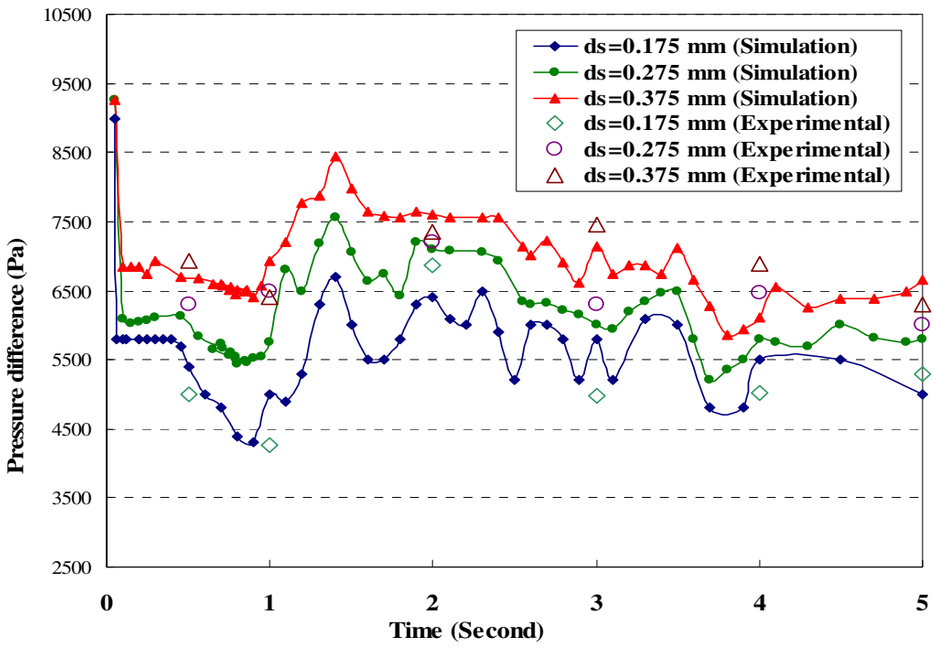

Fig. 9. Comparison of experimental and simulation bed pressure drop (P1-P2) at different solid particle sizes.

Comparison of experimental and simulated bed pressure drop (Pressure difference between two positions, P1-P2 and P1-P3) for two different particle sizes, d_s=0.175 mm and d_s=0.375 mm, at different superficial gas velocity are shown in Fig. 10. and Fig. 11. Pressure transducers positions (P1, P2, P3) also were shown in Fig. 4(B). The simulation and experimental results show better agreement at velocities above U_{mf}. The discrepancy for $U < U_{mf}$ may be attributed to the solids not being fluidized, thus being dominated by inter particle frictional forces, which are not predicted by the multi fluid model for simulating gas-solid phases.

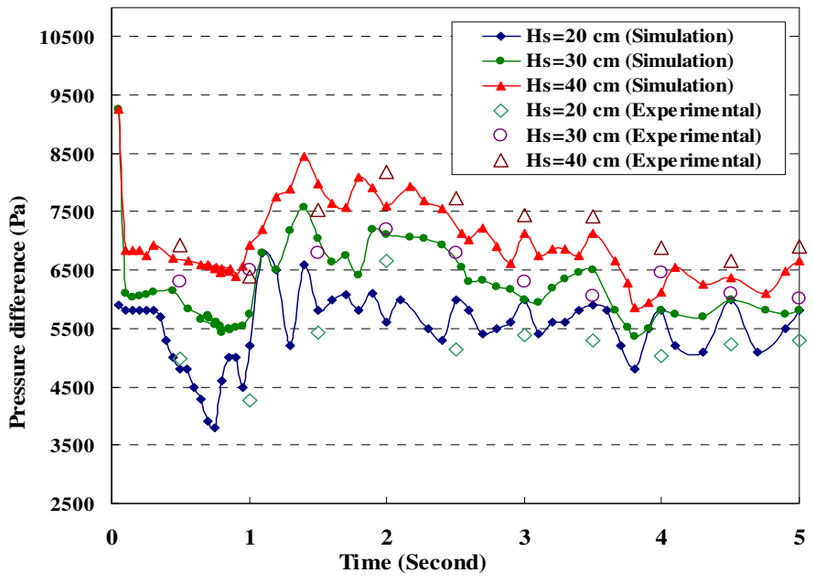

Fig. 10. Comparison of experimental and simulated bed pressure drop at different time

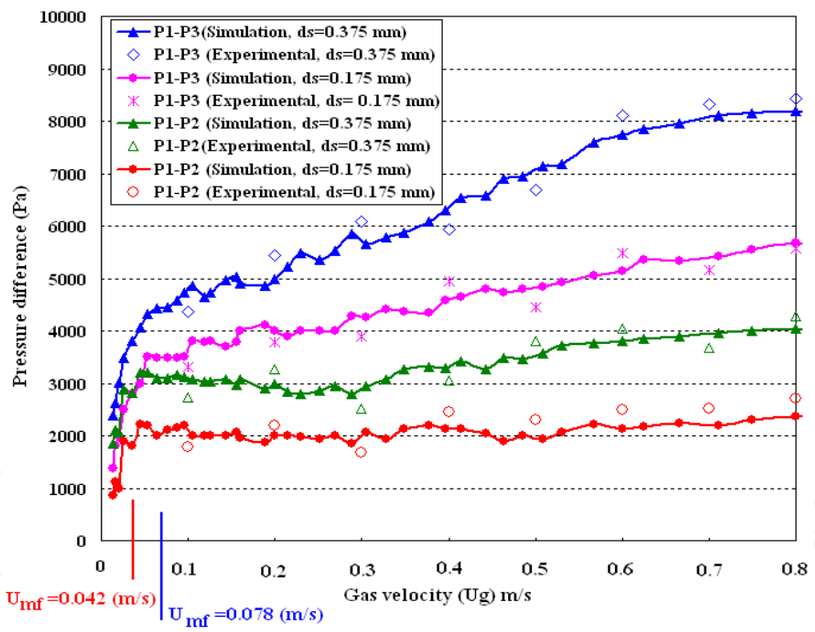

Fig. 11. Comparison of experimental and simulated bed pressure drop at different gas velocity and particle sizes.

Comparison of experimental and simulated bed pressure drop for two different initial bed height, H_s=30, H_s=40 cm, at different superficial gas velocity are shown in Fig. 11. The results show with increasing the initial static bed height and gas velocity, pressure drop (P1-P2 and P1-P3) increase but the rate of increasing for (P1-P3) is larger than (P1-P2). Comparison of the model predictions and experimental measurements on pressure drop (for both cases) show good agreement at different gas velocity.

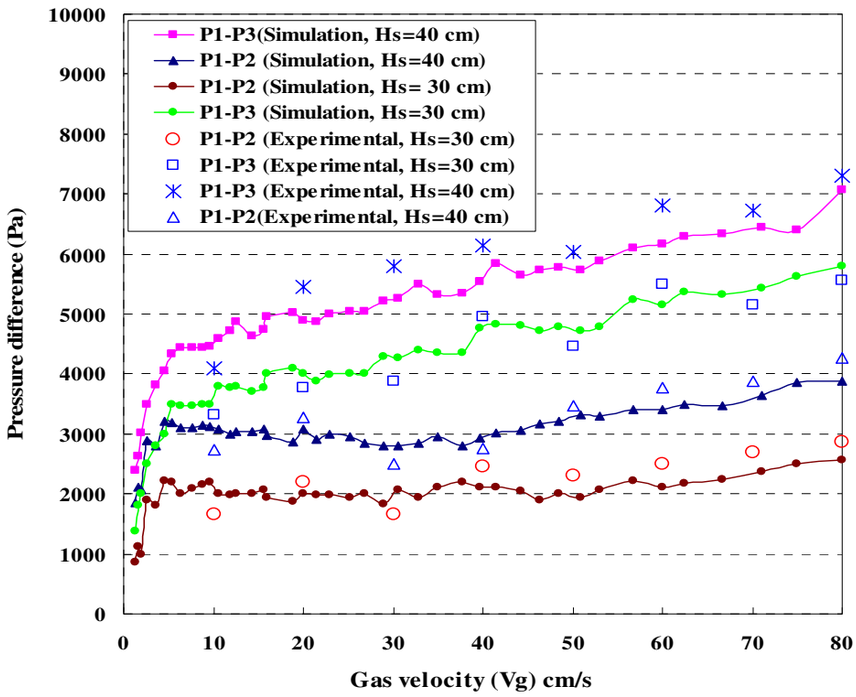

Fig. 12. Comparison of experimental and simulated bed pressure drop at different superficial gas velocity and static bed height.

These Figs. show that with increasing gas velocity, initially the pressure drops (P1-P2 and P1-P3) increase, but the rate of increase for (P1-P3) is larger than for (P1-P2). As indicated in Fig. 12. the bed overall pressure drop decreased significantly at the beginning of fluidization and then fluctuated around a near steady-state value after about 4 s. Pressure drop fluctuations are expected as bubbles continuously split and coalesce in a transient manner in the fluidized bed.

The results show with increasing the initial static bed height, pressure drop increase because of increasing the amount of particle, interaction between particle-particle and gas-particle. The results show with increasing the particle size, gas velocity and initial static bed height pressure drop (P1-P2 and P1-P3) increases. Comparison of the model predictions and experimental measurements on pressure drop (for both cases) show good agreement at different gas velocity.

The experimental data for time-averaged bed expansions as a function of superficial velocities are compared in Fig. 13 with the corresponding values predicted by the models using the Syamlal–O'Brien, Gidaspow and Cao-Ahmadi drag expressions. This Fig. shows that the models predict the correct increasing trend of the bed height with the increase of superficial gas velocity. There are, however, some deviations and the models slightly underpredict the experimental values. The amount of error for the bed expansion ratio for the Syamlal-O'Brien, the Gidaspow and Cao-Ahmadi models are, respectively, 6.7%, 8.7% and 8.8%. This Fig. suggests that the Syamlal–O'Brien drag function gives a somewhat better prediction when compared with the Gidaspow and Cao-Ahmadi models. In addition, the Syamlal–O'Brien drag law is able to more accurately predict the minimum fluidization velocity.

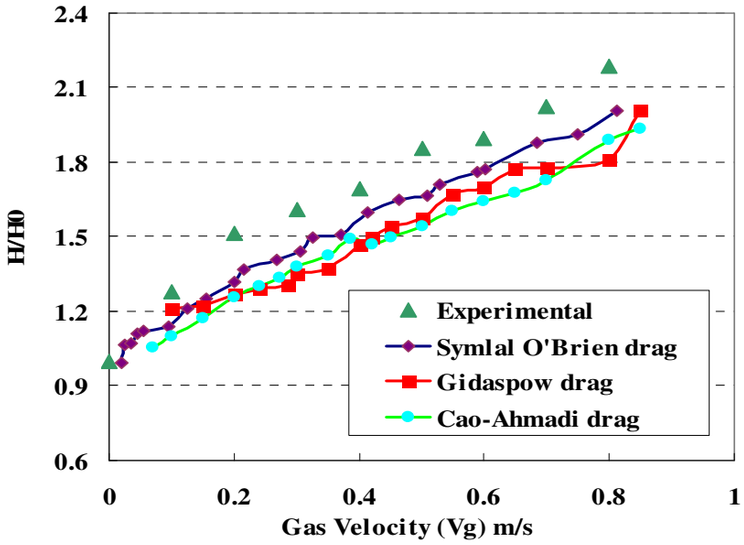

Fig. 13. Comparison of experimental and simulated bed expansion ratio.

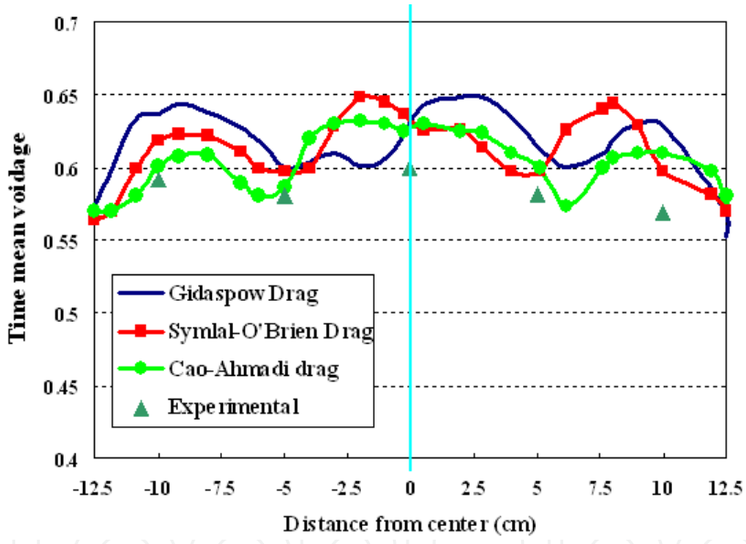

Fig. 14. Experimental and simulated time-averaged local voidage profiles at z=30 cm, Vg=50 cm/s.

The experimental data for the time-averaged voidage profile at a height of 30 cm is compared with the simulation results for the three different drag models in Fig. 14 for V_g=50 cm/s. This Fig. shows the profiles of time-averaged voidages for a time interval of 5 to 10 s. In this time duration, the majority of the bubbles move roughly in the bed mid-section toward the bed surface. This Fig. shows that the void fraction profile is roughly uniform in the core of the bed with a slight decrease near the walls. The fluctuation pattern in the void fraction profile is perhaps due to the development of the gas bubble flow pattern in the bed. Similar trends have been observed in the earlier CFD models of fluidized beds [8, 11]. The gas volume fraction average error between CFD simulations and the experimental data for the drag models of Gidaspow, Syamlal–O'Brien and Cao-Ahmadi are, respectively, about

12.7%, 7.6% and 7.2%. This observation is comparable to those of the earlier works [8, 11]. It can be seen that Cao- Ahmadi drag expression leads to a better prediction compared with those of Syamlal–O'Brien and Gidaspow drag models for the time averaged voidage.

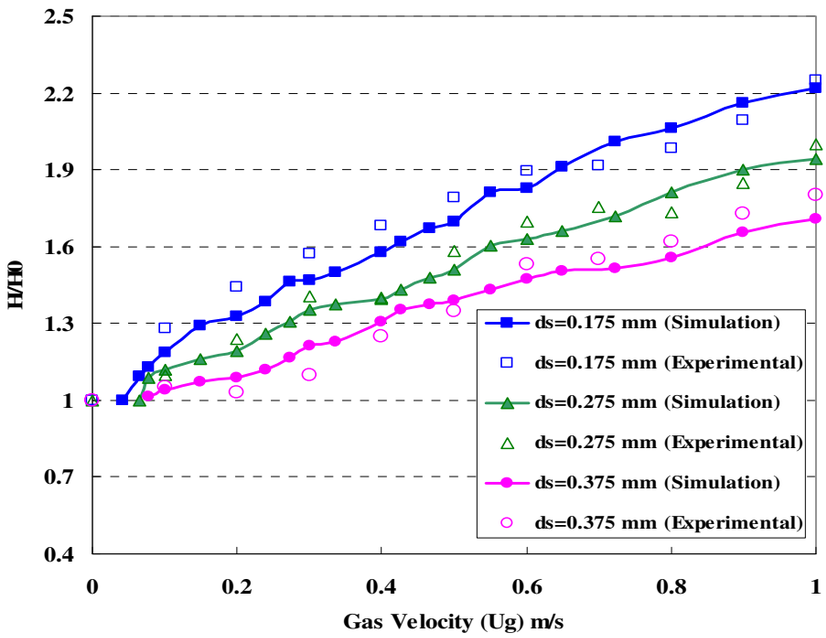

Fig. 15. Comparison of experimental and simulated bed expansion ratio for different solid particle sizes.

Time-averaged bed expansions as a function of superficial velocities are compared in Fig. 15. This Fig. shows that the model predicts the correct increasing trend of the bed height with the increase of superficial gas velocity. All cases demonstrate a consistent increase in bed expansion with gas velocity and predict the bed expansion reasonably well. There are, however, some deviations under predict the experimental values. This Fig. shows that with increasing the particles sizes, bed expansion ratio decreases. On the other hand, for the same gas velocity, bed expansion ratio is lager for smaller particles.

The experimental data of time-average bed expansion ratio were compared with corresponding values predicted for various velocities as depicted in Fig. 16. The time-average bed expansion ratio error between CFD simulation results and the experimental data for two different initial bed height, H_s=30, H_s=40 cm, are 6.7% and 8.7% respectively. Both cases demonstrate a consistent increase in bed expansion with gas velocity and predict the bed expansion reasonably well. It can be seen that Syamlal–O'Brien drag function gives a good prediction in terms of bed expansion and also, Syamlal–O'Brien drag law able to predict the minimum fluidization conditions correctly.

Simulation results for void fraction profile are show in Fig. 17. In this Fig. symmetry of the void fraction is observed at three different particle sizes. The slight asymmetry in the void fraction profile may result form the development of a certain flow pattern in the bed. Similar asymmetry has been observed in other CFD modeling of fluidized beds. Void fraction profile for large particle is flatter near the center of the bed. The simulation results of time-average cross-sectional void fraction at different solid particles diameter is shown in Fig. 18

for U_g=38 cm/s. This Fig. shows with increasing solid particles diameter, void fraction and bed height increase and steady state condition arrive rapidly.

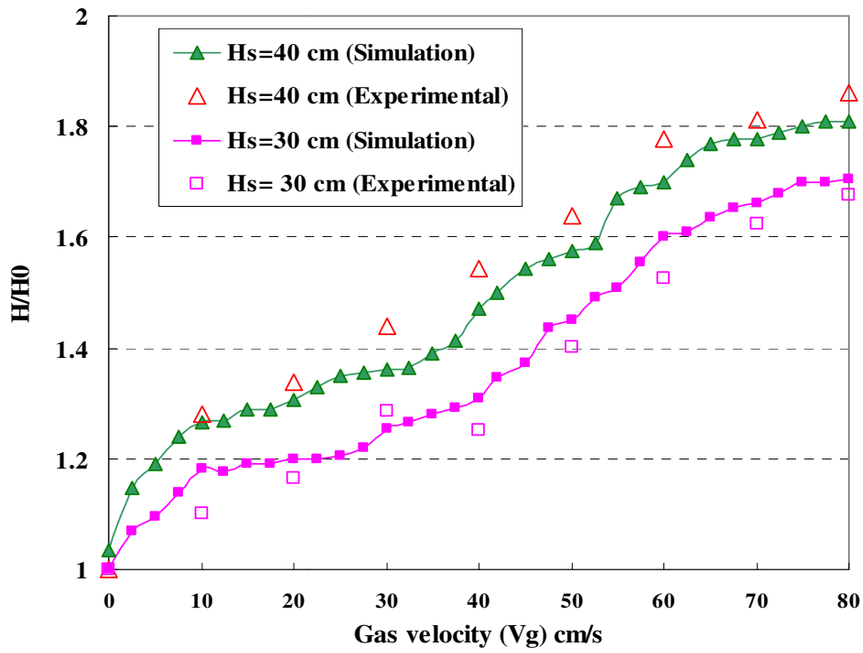

Fig. 16. Comparison of experimental and simulated bed expansion ratio for different initial static bed height.

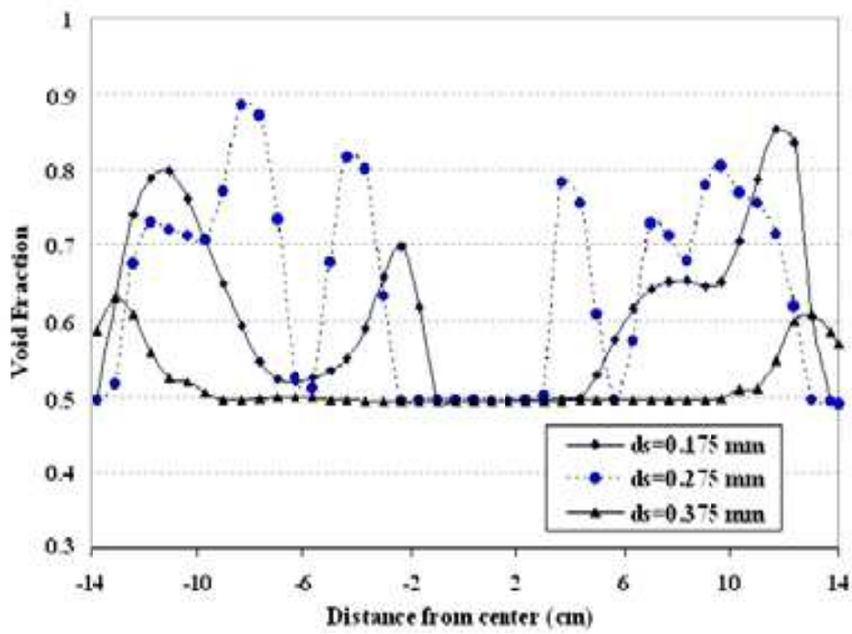

Fig. 17. Simulated void fraction at different solid particles diameter (at z=20 cm, Ug=38 cm/s, t=5.0s)

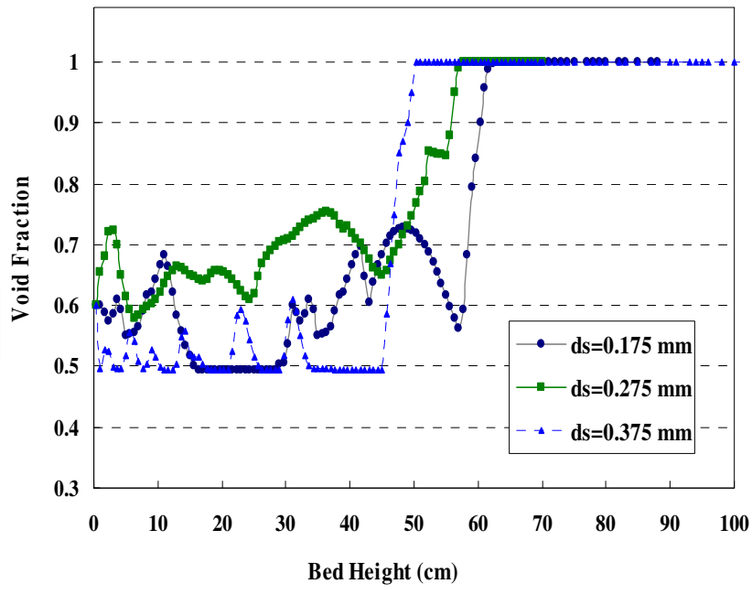

Fig. 18. Simulation results of time-average cross-sectional void fraction at different solid particles diameter (U_g=38cm/s)

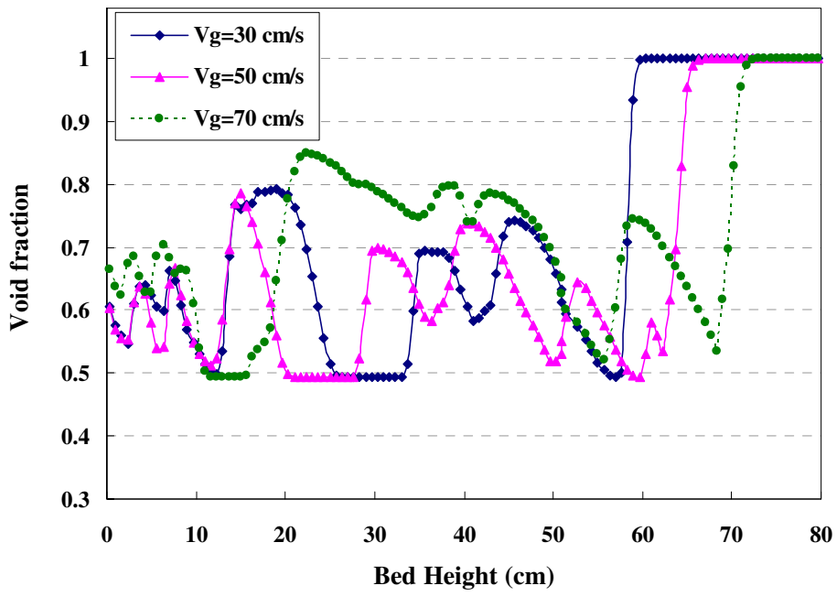

Fig. 19. Simulation results of time-average cross-sectional void fraction at different superficial gas velocity (H_s=40 cm)

Fig. 19 shows the simulation results of time-average cross-sectional void fraction, gas volume fraction, at different superficial gas velocity. This Fig. shows with increasing superficial gas velocity, void fraction also increase and bed arrive to steady state condition rapidly. Also in some position the plot is flat, it is means that particle distribution is uniform. When void fraction increase suddenly in the bed, it is means that the large bubble product in this position and when decrease, the bubble was collapsed.

Fig. 20 shows simulation results for void fraction contour plot, gas volume fraction, for U_g = 38 cm/s, d_s = 0.175 mm. The increase in bed expansion and variation of the fluid-bed voidage can be observed. At the start of the simulation, waves of voidage are created, which travel through the bed and subsequently break to form bubbles as the simulation progresses. Initially, the bed height increased with bubble formation until it leveled off at a steady-state bed height. The observed axisymmetry gave way to chaotic transient generation of bubble formation after 1.5 s. The bubbles coalesce as they move upwards producing bigger bubbles. The bubbles become stretched as a result of bed wall effects and interactions with other bubbles.

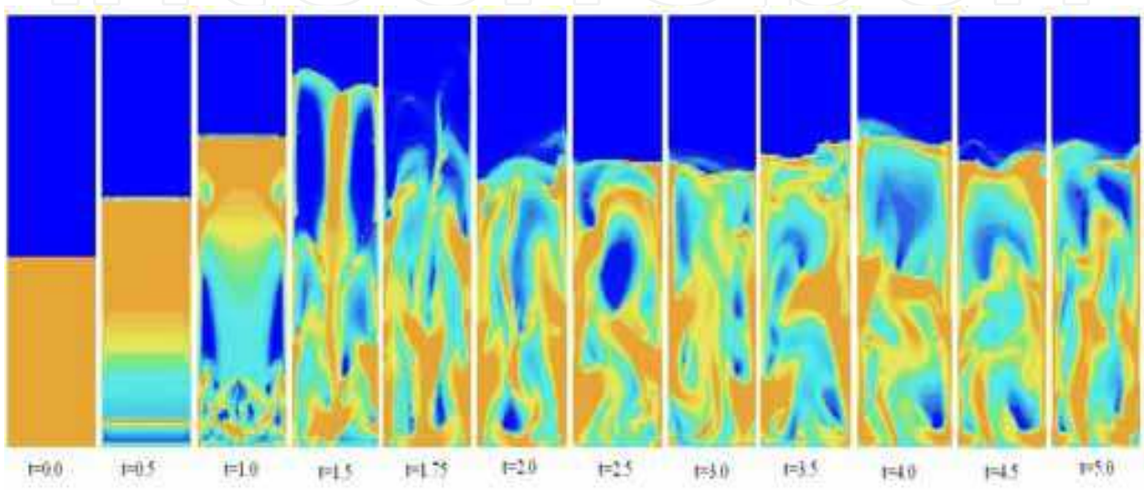

Fig. 20. Simulation void fraction profile of 2D bed (U_g= 38 cm/s, d_s = 0.175 mm)

The contour plots of solids fraction shown in Fig. 21 indicate similarities between the experimental and simulations for three particle sizes and at three different times. The results show that the bubbles at the bottom of the bed are relatively small. The experiments indicated small bubbles near the bottom of the bed; the bubbles grow as they rise to the top surface with coalescence. The elongation of the bubbles is due to wall effects and interaction with other bubbles. Syamlal–O'Brien drag model provided similar qualitative flow patterns. The size of the bubbles predicted by the CFD models are in general similar to those observed experimentally. Any discrepancy could be due to the effect of the gas distributor, which was not considered in the CFD modeling of fluid bed. In practice, jet penetration and hydrodynamics near the distributor are significantly affected by the distributor design.

The increase in bed expansion and the greater variation of the fluid-bed voidage can be observed in Fig. 20 and Fig. 21 for particles with d_s = 0.175 mm. According to experimental evidence, this type of solid particle should exhibit a bubbling behavior as soon as the gas velocity exceeds minimum fluidization conditions.

It is also worth noting that the computed bubbles show regions of voidage distribution at the bubble edge, as experimentally observed. In Fig. 21 symmetry of the void fraction is observed at three different particle sizes. The slight asymmetry in the void fraction profile may result form the development of a certain flow pattern in the bed. Similar asymmetry has been observed in other CFD modeling of fluidized beds [5, 8]. Void fraction profile for large particle is flatter near the center of the bed.

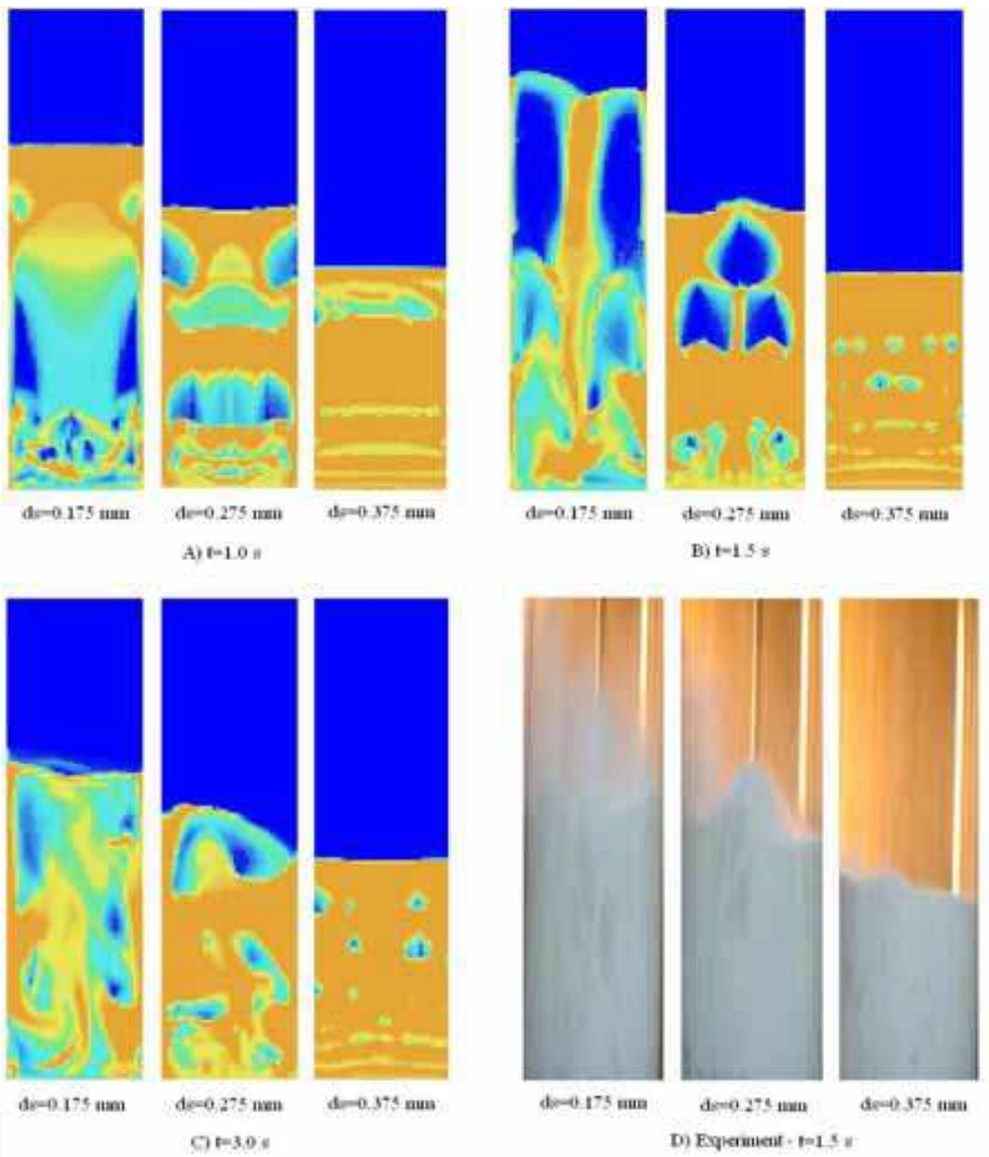

Fig. 21. Comparison of experiment and simulated void fraction and bobbles for three particle sizes and three different times

Fig. 22 shows simulated results for contour plot of solids volume fraction (U_g =38 cm/s, d_s=0.275 mm). Initially, the bed height increased with bubble formation until it leveled off at a steady-state bed height. The observed axisymmetry gave way to chaotic transient generation of bubble formation after 3 s. The results show that the bubbles at the bottom of the bed are relatively small. The bubbles coalesce as they move upwards producing bigger bubbles. The bubbles become stretched as a result of bed wall effects and interactions with other bubbles. Syamlal–O'Brien drag model provided similar qualitative flow patterns. The size of the bubbles predicted by the CFD models are in general similar to those observed experimentally. Any discrepancy could be due to the effect of the gas distributor, which was not considered in the CFD modeling of fluid bed. In practice, jet penetration and hydrodynamics near the distributor are significantly affected by the distributor design.

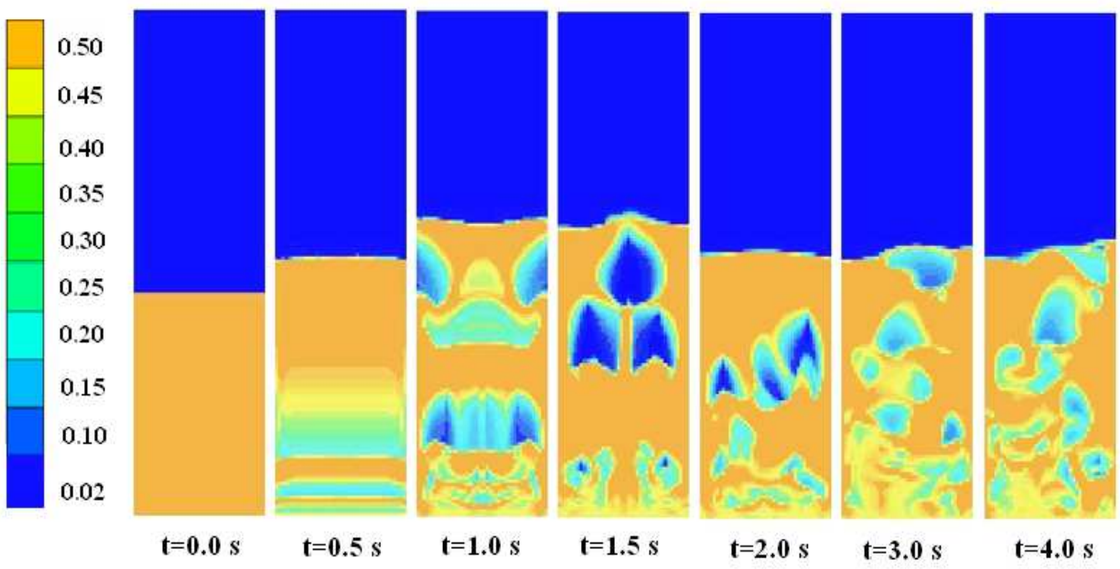

Fig. 22. Simulated solids volume fraction profile of 2D bed *(Ug*=38 cm/s, d_s=0.275 mm).

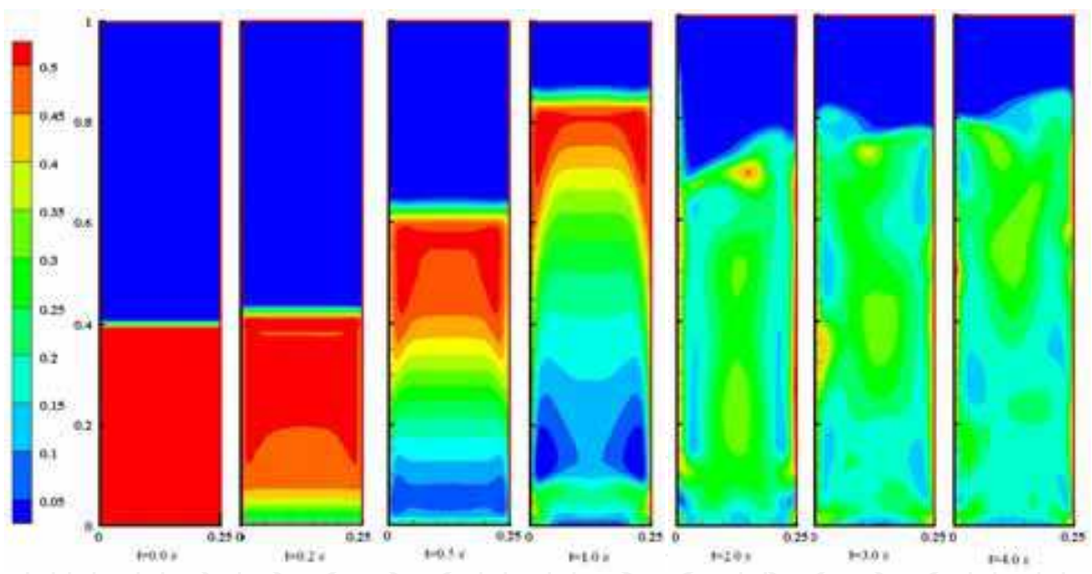

Fig. 23. Simulated solid volume fraction contours in the 2D bed *(Vg* =50 cm/s, drag function: Syamlal–O'Brien).

Simulation results for solid particle velocity vector fields at different times are shown in Fig. 24. This Fig. shows that initially the particles move vertically; at t= 0.7 s, two bubbles are formed in the bed that are moved to the upper part of the column. The bubbles collapse when they reach the top of the column, and solid particle velocity vector directions are changed as the particles move downward. The upward and downward movement of particles in the bed leads to strong mixing of the phases, which is the main reason for the effectiveness of the fluidized bed reactors.

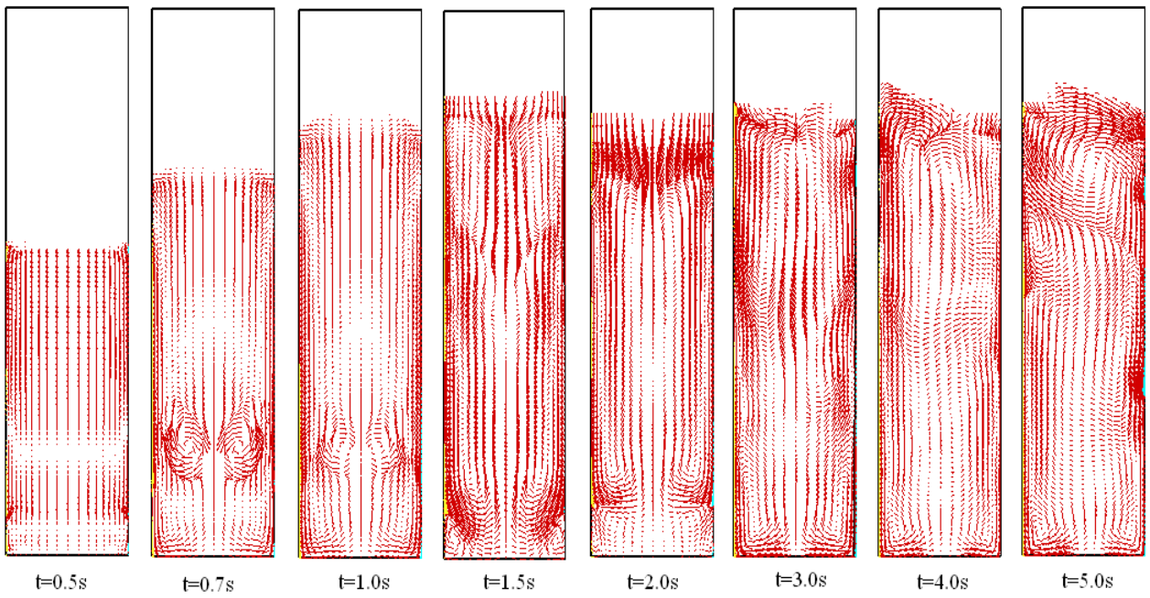

Fig. 24. Simulated solid particle velocity vector fields for different times, Vg=50 cm/s.

Fig. 25 compares the experimental results for bubble formation and bed expansion for different superficial gas velocities. At low gas velocities (lower than Vg=5.5 cm/s), the solids rest on the gas distributor, and the column is in the fixed bed regime. When superficial gas velocity reaches the fluidization velocity of 5.5 cm/s, all particles are entrained by the upward gas flow and the bed is fluidized. At this point, the gas drag force on the particles counterbalances the weight of the particles. When the gas velocity increases beyond the minimum fluidization velocity, a homogeneous (or smooth) fluidization regime forms in the bed. Beyond a gas velocity of 7 cm/s, a bubbling regime starts. With an increase in velocity beyond the minimum bubbling velocity, instabilities with bubbling and channeling of gas in the bed are observed. Vg=10 cm/s in Fig. 25 corresponds to this regime. At high gas velocities, the movement of solids becomes more vigorous. Such a bed condition is called a bubbling bed or heterogeneous fluidized bed, which corresponds to Vg=20-35 cm/s in Fig. 25. In this regime, gas bubbles generated at the distributor coalesce and grow as they rise through the bed. With further increase in the gas velocity (Vg=40-50 cm/s in Fig. 25), the intensity of bubble formation and collapse increases sharply. This in turn leads to an increase in the pressure drop as shown in Fig.s 8-11. At higher superficial gas velocities, groups of small bubbles break free from the distributor plate and coalesce, giving rise to small pockets of air. These air pockets travel upward through the particles and burst out at the free surface of the bed, creating the appearance of a boiling bed. As the gas bubbles rise, these pockets of gas interact and coalesce, so that the average gas bubble size increases with distance from the distributor. This bubbling regime for the type of powder studied occurs only over a narrow range of gas velocity values. These gas bubbles eventually become large enough to spread across the vessel. When this happens, the bed is said to be in the slugging regime. Vg=60 cm/s in Fig. 25 corresponds to the slugging regime. With further increase in the gas superficial velocity, the turbulent motion of solid clusters and gas bubbles of various size and shape are observed. This bed is then considered to be in a turbulent fluidization regime, which corresponds to Vg=70-100 cm/s in Fig. 25.

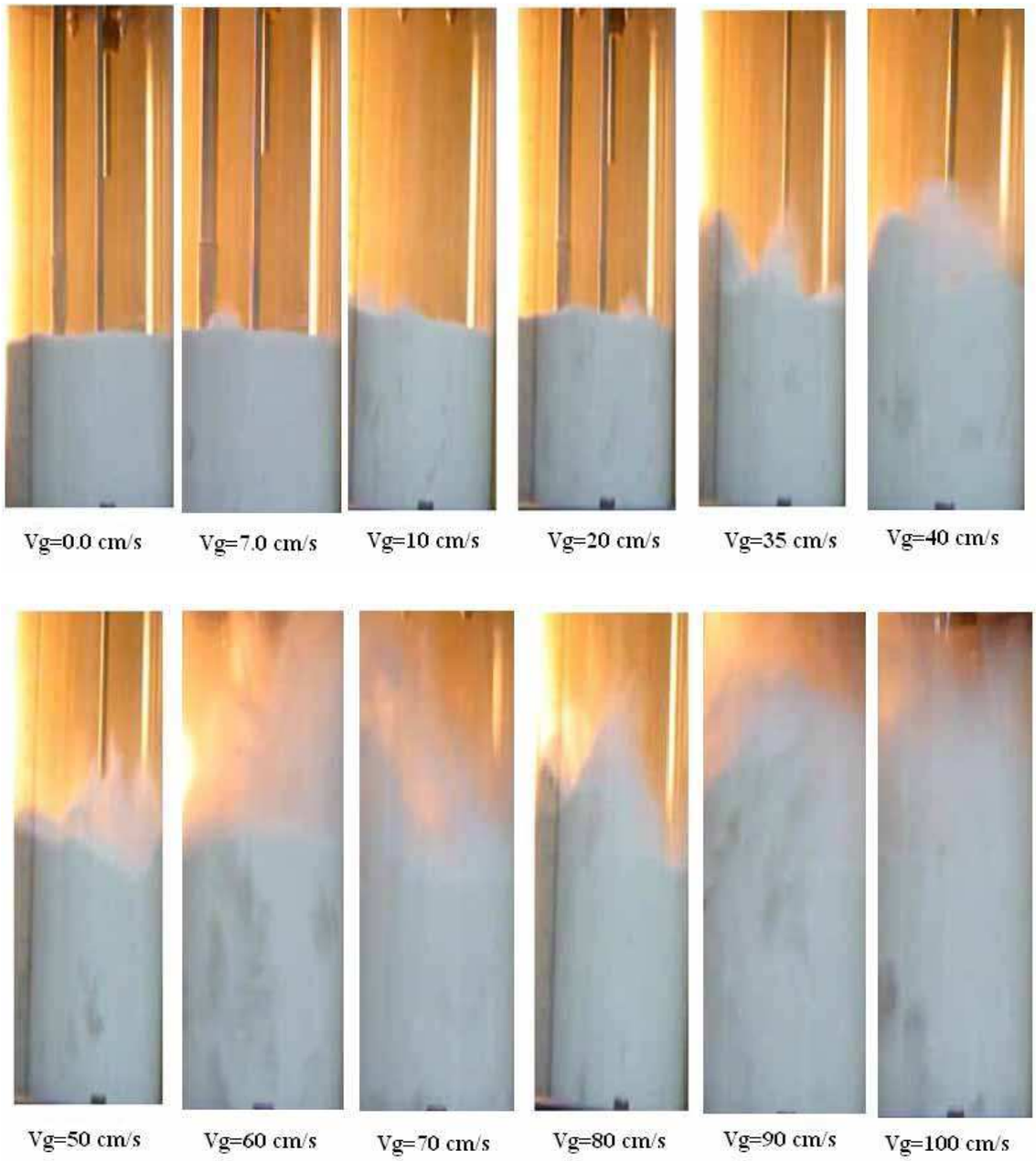

Fig. 25. Comparison of bubble formation and bed expansion for different superficial gas velocities.

Comparison of the contour plots of solid fractions in Fig. 24 and the experimental results for bubble formation and bed expansion in Fig. 25 for Vg=50 cm/s indicates qualitative similarities of the experimental observations and the simulation results. It should be pointed out that some discrepancies due to the effect of the gas distributor, which was not considered in the CFD model, should be expected.

Fig. 26 shows the simulation results of gas volume fraction for different superficial gas velocities. Initially, the bed height increases with bubble formation, so gas volume fraction

increases and levels off at a steady-state bed height. At the start of the simulation, waves of voidage are created, which travel through the bed and subsequently break to form bubbles as the simulation progresses. At the bottom of the column, particle concentration is larger than at the upper part. Therefore, the maximum gas volume fraction occurs at the top of the column. Clearly the gas volume fraction of 1 (at the top of the bed) corresponds to the region where the particles are absent. With increasing superficial gas velocity, Fig. 26 shows that the gas volume fraction generally increases in the bed up to the height of 50 to 60 cm. The gas volume fraction then increases sharply to reach to 1 at the top of the bed. Gas volume fraction approaches the saturation condition of 1 at the bed heights of 63cm, 70cm and 85 cm for Vg=30 cm/s, 50 cm/s and 80 cm/s, respectively. For higher gas velocities, Fig. 26 shows that the gas volume fraction is larger at the same height in the bed. This is because the amount of particles is constant and for higher gas velocity, the bed height is higher. Thus, the solid volume fraction is lower and gas volume fraction is higher. It should be noted here that the fluctuations of the curves in this Fig. are a result of bubble formation and collapse.

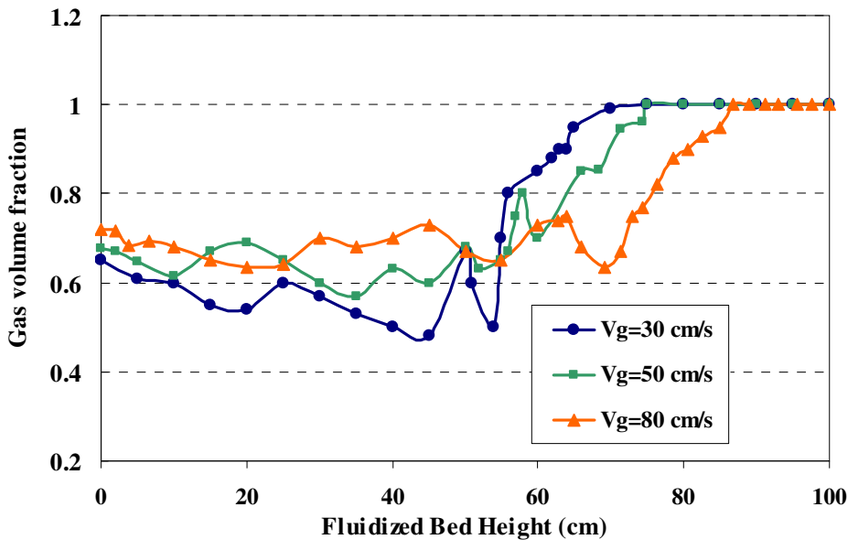

Fig. 26. Simulation results for gas volume fraction at t=5s (Syamlal–O'Brien drag model).

The influence of inlet gas velocity on the gas temperature is shown in Fig.s 27 and 28. As noted before, the gas enters the bed with a temperature of 473K, and particles are initially at 300K. Thermocouples are installed along the column as shown in Fig. 2(B). The thermocouple probes can be moved across the reactor for measuring the temperature at different radii. At each height, gas temperatures at five radii in the reactor were measured and averaged. The corresponding gas mean temperatures as function of height are presented in Fig.s 27 and 28. Fig. 29 shows that the gas temperature deceases with height because of the heat transfer between the cold particles and hot gas. Near the bottom of column, solid volume fraction is relatively high; therefore, gas temperature decreases rapidly and the rate of decrease is higher for the region near the bottom of the column. At top of the column, there are no particles (gas volume fraction is one) and the wall is adiabatic; therefore, the gas temperature is roughly constant. Also the results show that with increasing the gas velocity, as expected the gas temperature decreases. From Fig.s 22-25 it is seen that with increasing gas velocity, bed expansion height increases.

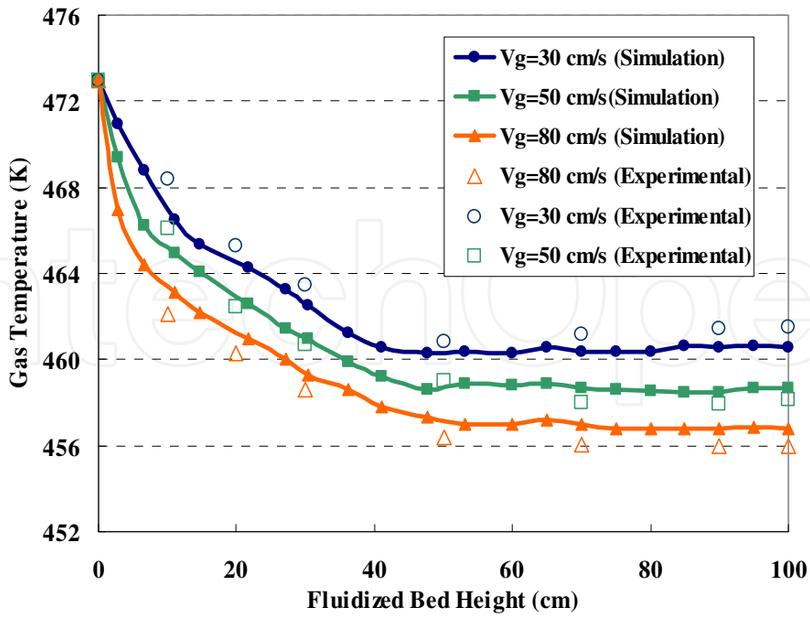

Fig. 27. Simulation and experimental results for inlet gas velocity effect on gas temperature in the bed (t=5 min).

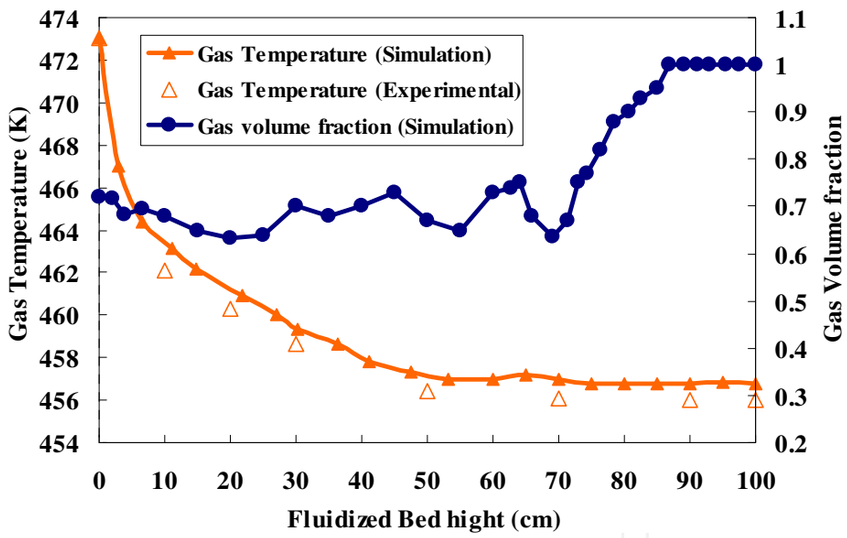

Fig. 28. Comparison of simulation and experimental gas temperature and gas volume fraction at t=5min for Vg=80 cm/s.

In addition, the gas temperature reaches to the uniform (constant temperature) condition in the upper region. When gas velocity is 30 cm/s, temperature reaches to its constant value at a height of about 40 cm; and for Vg=50 cm/s and Vg=80 cm/s, the corresponding gas temperatures reaching uniform state, respectively, at heights of 50 and 55 cm. Fig. 27 also shows that the simulation results are in good agreement with the experimental data. The small differences seen are the result of the slight heat loss from the wall in the experimental reactor. Fig. 28 shows the gas temperature and the gas volume fraction in the same graph.

This Fig. indicates that in the region where the gas volume fraction is highest, the gas temperature is lowest. Clearly in the free gas flow, there is little heat transfer. In the lower part of the reactor, the solid volume fraction is higher, so the rate of heat transfer with the cooler particles is higher and the temperature decreases faster.

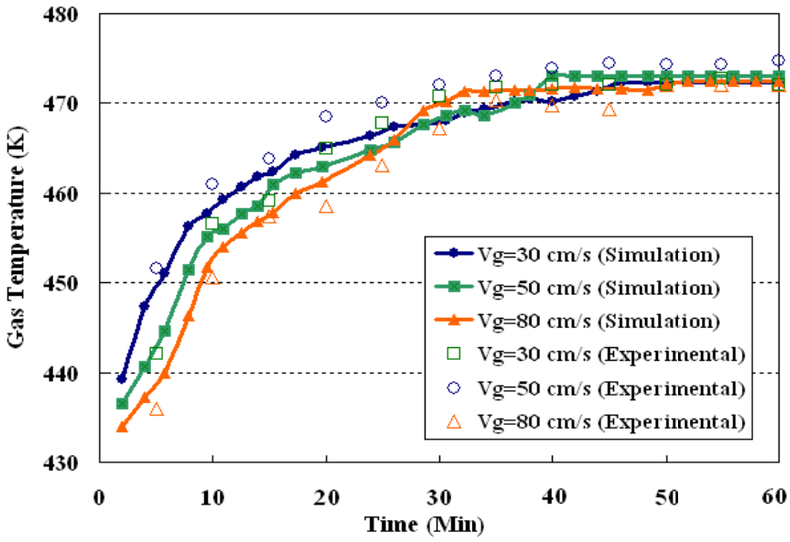

Fig. 29. Comparison of experimental and computational results for gas temperatures at different gas velocities (z=50 cm).

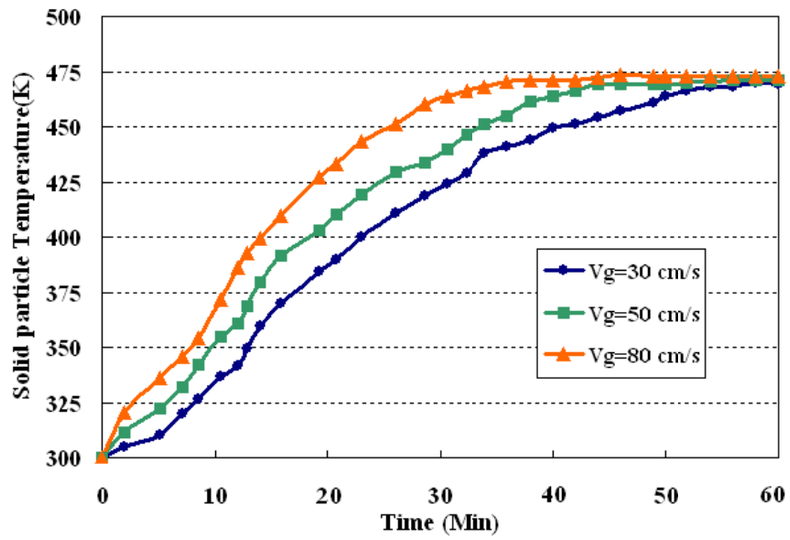

Fig. 30. Simulation results for variation of solid particle temperature with time at different gas velocities at z=50 cm

Fig. 29 compares the time variation of the simulated gas temperature at z=50 cm for different gas velocities with the experimental data. This Fig. shows that gas temperature increases with time and the rate of increase varies with somewhat with the gas velocity. The simulation results show that with increasing gas velocity, gas temperature reaches steady

state condition rapidly. For Vg=80 cm/s, gas temperature reaches steady state condition after about 30 min; but for Vg=50 and 30 cm/s temperature reaches to steady after 40 and 45min, respectively but there are a few difference between simulation and experimental results.

For different inlet gas velocities, time variations of the mean solid phase temperature at the height of z=50 cm are shown in Fig. 30. The corresponding variation of the averaged solid particle temperature with height is shown in Fig. 31. Note that, here, the averaged solid temperature shown is the mean of the particle temperatures averaged across the section of the column at a given height. It is seen that the particle temperature increases with time and with the distance from the bottom of the column. Fig. 30 also shows that at higher gas velocity, solid temperature more rapidly reaches the steady state condition. For Vg=80cm/s, solid temperature approaches the steady limit after about 30min; for Vg=50 and 30 cm/s, the steady state condition is reached, respectively, at about 40 and 45min. In addition, initially the temperature differences between solid and gas phases are higher; therefore, the rate of increase of solid temperature is higher. Fig. 31 shows that the rate of change of the solid temperature near the bottom of the bed is faster, which is due to a larger heat transfer rate compared to the top of the bed. These Fig.s also indicate that an increase in the gas velocity causes a higher heat transfer coefficient between gas and solid phases, and results in an increase in the solid particle temperature.

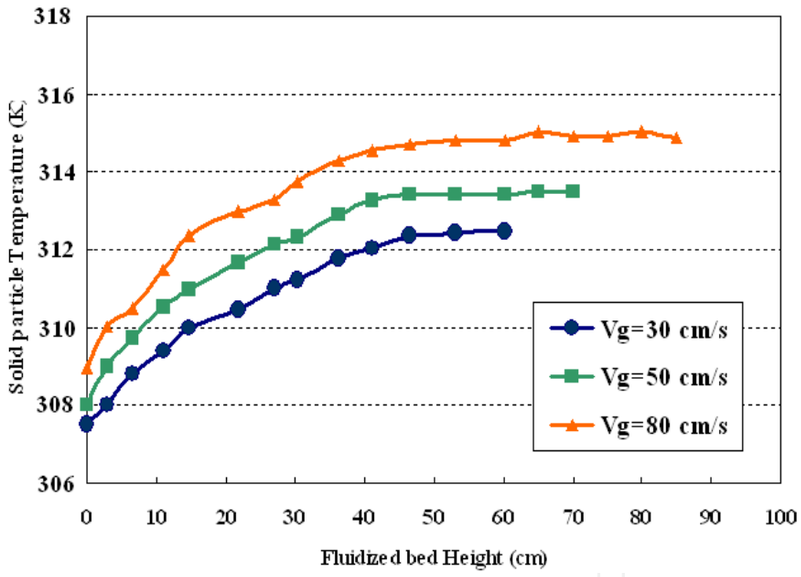

Fig. 31. Inlet gas velocity effect on the simulated solid particle temperatures in bed (t=5min).

The influence of initial bed height (particle amount) on the gas temperature at t=5s is shown in Fig. 32 experimentally and computationally. It indicates that with increasing the particle amount, due to a higher contact surfaces and heat transfer between hot gas and cold solid phase, gas temperature decreases.

The rate of gas temperature decreasing for H_s=40 cm is larger than H_s=20 cm because with increasing the particle amount, volume of cold solid particles and contact surface with hot gas increase. The effects of static initial bed height on solid phase temperature are shown in Fig. 33. It indicates that a decrease in particle amount causes a higher void fraction, gas volume fraction, and heat transfer coefficient between gas and solid phases (resulting in a

higher contact surface between hot gas and cold solid phase) that in turn leads to an increase in solid particle temperature. So with increasing the initial bed height from 20cm to 40cm, gas temperature decreases (Fig. 32) and solid phase temperature increases and rate of this increasing for Hs=40cm is larger than others (Fig. 33). Comparison of the model predictions and experimental measurements on mean gas temperature show good agreement for most operating conditions.

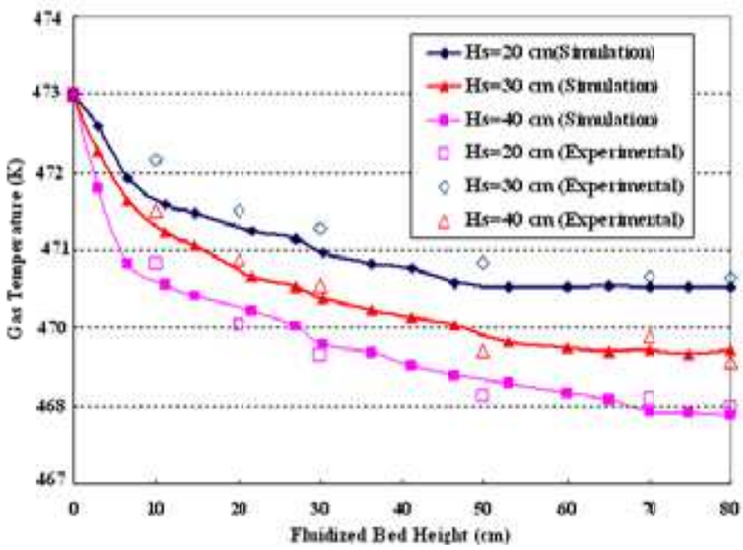

Fig. 32. Comparison of simulation and experimental results of bed height effect on gas temperature at t=5s (Vg=50 cm/s).

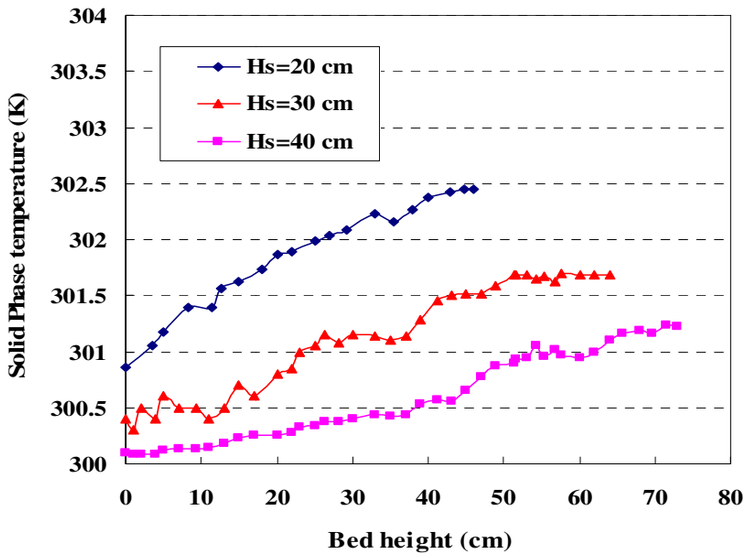

Fig. 33. Simulation results of initial bed height effect on solid particle temperature at t=5s (Vg=50 cm/s).

In addition, the temperature gradient between solid and gas phases is higher at the bed because inlet gas temperature is the highest and solid particles temperature is lowest in the

bed. The slope of temperature plots is higher at the top of the bed due to larger gas volume fraction that leads to a larger contact surfaces and heat transfer rate compared to the bottom of the bed. The influence of inlet gas velocity on the gas temperature is showed in Fig. 34. It indicates that with increasing the gas velocity, due to higher heat transfer coefficient between gas and solid phases, gas temperature decrease rapidly and also rate of this decreasing with increasing the gas velocity increase rapidly. The modeling predictions compared reasonably well with experimental data.

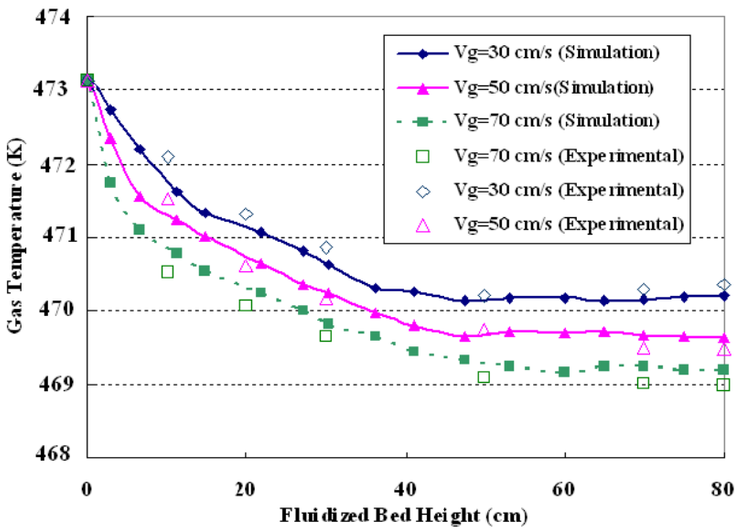

Fig. 34. Comparison of experimental and computational results of gas temperature at different gas velocity (H_s=40 cm, t=5s)

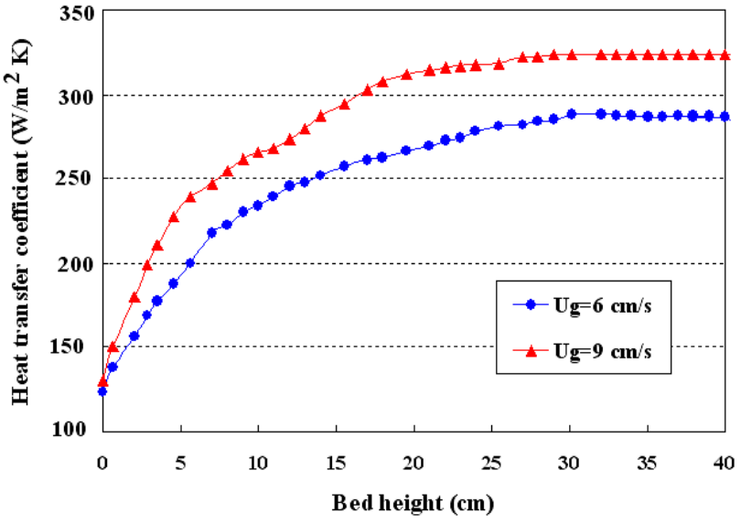

Fig. 35. Simulation results for heat transfer coefficient at different gas velocities (t=7 s).

Simulation results for heat transfer coefficient at different gas velocities at t=7s are shown in Fig. 35. From results of this Fig., heat transfer coefficient increases from bottom to top in the

column because with results of Fig. 35. gas volume fraction increases from bottom to top. This Fig. also indicates that an increase in the gas velocity causes a higher heat transfer coefficient between gas and solid phases.

6. Conclusions

In this chapter, unsteady flow and heat transfer in a gas–solid fluidized bed reactor was investigated. Effect of different parameters for example superficial gas velocity and temperature, initial static bed height and solid particles diameter on hydrodynamics of a two-dimensional gas–solid fluidized bed reactor was studied experimentally and computationally. The Eulerian-Eulerian model with the standard k - ε turbulence model was used for modeling the fluidized bed reactor. The model includes continuity, momentum equations, as well as energy equations for both phases and the equations for granular temperature of the solid particles. A suitable numerical method that employed finite volume method was applied to discritize the governing equations. In order to validate the model, an experimental setup was fabricated and a series of tests were performed. The predicted time-average bed expansion ratio, pressure drop and cross-sectional voidage profiles using Cao-Ahmadi, Syamlal–O'Brien and Gidaspow drag models were compared with corresponding values of experimentally measured data. The modeling predictions compared reasonably well with the experimental bed expansion ratio measurements and qualitative gas–solid flow patterns. Pressure drops predicted by the simulations were in relatively close agreement with the experimental measurements for superficial gas velocities higher than the minimum fluidization velocity. Results show that there is no significant difference for different drag models, so the results suggest that all three drag models are more suitable for predicting the hydrodynamics of gas–solid flows. The simulation results suggested that the Syamlal–O'Brien drag model can more realistically predict the hydrodynamics of gas–solid flows for the range of parameters used in this study. Moreover, gas and solid phase temperature distributions in the reactor were computed, considering the hydrodynamics and heat transfer of the fluidized bed using Syamlal–O'Brien drag expression. Experimental and numerical results for gas temperature showed that gas temperature decreases as it moves upwards in the reactor. The effects of inlet gas velocity, solid particles siizes and initial static bed height on gas and solid phase temperature was also investigated. The simulation showed that an increase in the gas velocity leads to a decrease in the gas and increase in the solid particle temperatures. Furthermore, comparison between experimental and computational simulation showed that the model can predict the hydrodynamic and heat transfer behavior of a gas-solid fluidized bed reasonably well.

7. Acknowledgments

The authors would like to express their gratitude to the Fluid Mechanics Research Center in Department of Mechanical Engineering of Amirkabir University, National Petrochemical company (NPC) and the Petrochemistry Research and Technology Company for providing financial support for this study.

8. Appendix

In this section drive an algebraic (discretized) equation from a partial differential equation [39, 40].

Continuity equation

For this demonstration the transport equation for a scalar ϕ is (m = 0, 1 for solid and gas phases):

$$\frac{\partial}{\partial t}(\alpha_m \rho_m \phi) + \frac{\partial}{\partial x_i}(\alpha_m \rho_m v_{mi} \phi) = 0 \tag{A1}$$

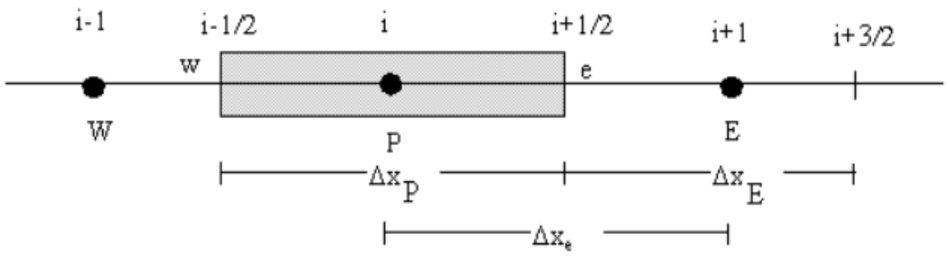

Fig. A1. Control volume and node locations in x-direction

With integrating this Equation over a control volume (Fig. A1) and write term by term, from left to right as follows:

Transient term

$$\int \frac{\partial}{\partial t}(\alpha_m \rho_m \phi) dV \approx [(\alpha_m \rho_m \phi)_P - (\alpha_m \rho_m \phi)_P^o] \frac{\Delta V}{\Delta t} \tag{A2}$$

where the superscript 'o' indicates old (previous) time step values.

Convection term

$$\begin{gathered}\int \frac{\partial}{\partial x_i}(\alpha_m \rho_m v_{mi} \phi)\, dV \approx \{\xi_e(\alpha_m \rho_m \phi)_E + \bar{\xi}_e(\alpha_m \rho_m \phi)_P\}(u_m)_e A_e \\ \{\xi_w(\alpha_m \rho_m \phi)_P + \bar{\xi}_w(\alpha_m \rho_m \phi)_W\}(u_m)_w A_w + \{\xi_n(\alpha_m \rho_m \phi)_N + \bar{\xi}_n(\alpha_m \rho_m \phi)_P\}(v_m)_n A_n \\ - \{\xi_s(\alpha_m \rho_m \phi)_P + \bar{\xi}_s(\alpha_m \rho_m \phi)_S\}(v_m)_s A_s\end{gathered} \tag{A3}$$

Combining the equations derived above Discretized Transport Equation is get

$$\begin{gathered}\left(\frac{(\rho'_m \phi)_P - (\rho'_m \phi)^0}{\Delta t}\right) \Delta V + \{\xi_e(\rho'_m \phi)_E + \bar{\xi}_e(\rho'_m \phi)_P\}(u_m)_e A_e - \\ \{\xi_w(\rho'_m \phi)_P + \bar{\xi}_w(\rho'_m \phi)_W\}(u_m)_w A_w + \{\xi_n(\rho'_m \phi)_N + \bar{\xi}_n(\rho'_m \phi)_P\}(v_m)_n A_n - \\ \{\xi_s(\rho'_m \phi)_P + \bar{\xi}_s(\rho'_m \phi)_S\}(v_m)_s A_s = 0\end{gathered} \tag{A4}$$

where the macroscopic densities define as $\rho'_m = \alpha_m \rho_m$

Equation (A4) may be rearranged to get the following linear equation for ϕ , where the subscript nb represents E, W, N and S [39, 40].

$$a_P \phi_P = \sum_{nb} a_{nb} \phi_{nb} + b \quad , \quad a_P = \sum_{nb} a_{nb} \tag{A5}$$

The discretized form of continuity equation can be easily by setting $\phi = 1$ and a linear equation of the form (A4), in which the coefficients are defined as follows:

$$a_E = -\xi_e(\alpha_m \rho_m)_E (u_m)_e A_e \quad a_W = \bar{\xi}_w(\alpha_m \rho_m)_W (u_m)_w A_w \tag{A6}$$

$$a_N = -\xi_n(\alpha_m\rho_m)_N(v_m)_n A_n \quad a_S = \bar{\xi}_s(\alpha_m\rho_m)_S(v_m)_s A_s \tag{A7}$$

$$a_P = \sum_{nb} a_{nb} + a_P^0 \quad a_P^0 = \frac{(\alpha_m\rho_m)^0}{\Delta t}\Delta V \quad b = a_P^0\phi_P^0 \tag{A8}$$

Momentum equation

The discretization of the momentum equations is similar to that of the scalar transport equation, except that the control volumes are staggered. As explained by Patankar, if the velocity components and pressure are stored at the same grid locations a checkerboard pressure field can develop as an acceptable solution. A staggered grid is used for preventing such unphysical pressure fields. As shown in Fig.A2, in relation to the scalar control volume centered around the filled circles, the x-momentum control volume is shifted east by half a cell. Similarly the y-momentum control volume is shifted north by half a cell, control volume is shifted top by half a cell.

For calculating the momentum convection, velocity components are required at the locations E, W, N, and S. They are calculated from an arithmetic average of the values at neighboring locations [39, 40]:

$$(u_m)_E = f_E(u_m)_P + (1 - f_E)(u_m)_e \tag{A9}$$

$$(v_m)_N = f_p(v_m)_{NW} + (1 - f_P)(v_m)_{NE} \tag{A10}$$

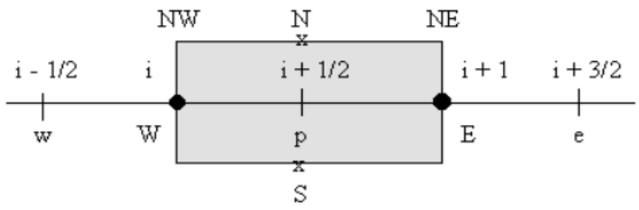

Fig. A2. X-momentum equation control volume

A volume fraction value required at the cell center denoted by *p* is similarly calculated.

$$(\alpha_m)_P = f_P(\alpha_m)_W + (1 - f_P)(\alpha_m)_E \tag{A11}$$

$$f_E = \frac{\Delta x_{Ee}}{\Delta x_P + \Delta x_e} \quad f_P = \frac{\Delta x_E}{\Delta x_W + \Delta x_E} \tag{A12}$$

Now the discretized x-momentum equation can be written as

$$a_P(u_m)_P = \sum_{nb} a_{nb}(u_m)_{nb} + b_P - A_P(\alpha_m)_P\left(\left(P_g\right)_E - \left(P_g\right)_W\right) + (\beta_{gs}(u_g - u_s)_P)\Delta V_e \tag{A13}$$

The above equation is similar to the discretized scalar transport equation , except for the last two terms: The pressure gradient term is determined based on the current value of Pg and is added to the source term of the linear equation set. The interface transfer term couples all the equations for the same component.

The definitions for the rest of the terms in Equation (A13) are as follows:

$$a_e = D_E - \xi_E(\alpha_m\rho_m)_e(u_m)_E A_E \qquad a_w = D_W + \bar{\xi}_W(\alpha_m\rho_m)_w(u_m)_W A_W \tag{A14}$$

$$a_n = D_N - \xi_N(\alpha_m\rho_m)_n(v_m)_N A_N \qquad a_s = D_S + \bar{\xi}_S(\alpha_m\rho_m)_s(v_m)_S A_S \tag{A15}$$

$$a_P = \sum_{nb} a_{nb} + a_P^0 + S' \qquad b = a_P^0 u_m^0 + (\alpha_m\rho_m)_e g_x \Delta V_e + \bar{S} \tag{A16}$$

$$a_P^0 = \frac{(\alpha_m\rho_m)^0\Delta V_e}{\Delta t} \qquad D_E = \frac{(\mu_m)_E A_E}{\Delta x_E} \tag{A17}$$

The center coefficient *ap* and the source term b contain the extra terms S' and $\bar{S}$, which account for the sources arising from shear stress terms.

Fluid pressure correction equation

An important step in the algorithm is the derivation of a discretization equation for pressure, which is described in this section. As stated, first momentum equations are solved using the pressure field P_g^* and the void fraction field ϵ_0^* from the previous iteration to calculate tentative values of the velocity fields u_s^* and u_g^* and other velocity components. The actual values differ from the (starred) tentative values by the following corrections

$$\left(P_g\right)_E = \left(P_g^*\right)_E + \left(P_g'\right)_E \qquad (P_s)_E = (P_s^*)_E + (P_s')_E \tag{A18}$$

$$(u_0)_p = (u_0^*)_p + (u_0')_p \qquad (u_1)_p = (u_1^*)_p + (u_1')_p \tag{A19}$$

To develop an approximate equation for fluid pressure correction, the momentum convection and solids pressure terms are dropped to get (m = 0, 1 for solid and gas phases)

$$a_{0p}(u_0')_p = \sum_{nb} a_{0nb}(u_0')_{nb} - A_p(\alpha_0^*)_p\left(\left(P_g'\right)_E - \left(P_g'\right)_W\right) + \beta_{10}\left[(u_1')_p - (u_0')_p\right]\Delta V \tag{A20}$$

$$\begin{aligned} a_{1p}(u_1')_p = {} & \sum_{nb} a_{1nb}(u_1')_{nb} - A_p(\alpha_1^*)_p\left(\left(P_g'\right)_E - \left(P_g'\right)_W\right) \\ & + \beta_{10}\left[(u_0')_p - (u_1')_p\right]\Delta V - A_p((P_s')_E - (P_s')_W) \end{aligned} \tag{A21}$$

Substituting the above equation and similar equations for other components of velocity into the fluid continuity equation an equation for pressure correction get.

$$\begin{aligned} & \left(\frac{(\alpha_0\rho_0)_P - (\alpha_0\rho_0)_P^0}{\Delta t}\right)\Delta V + \left\{(\alpha_0\rho_0)_E\xi_e + (\alpha_0\rho_0)_P\bar{\xi}_e\right\}\left[(u_0^*)_e - d_{0e}\left(\left(P_g'\right)_E - \left(P_g'\right)_P\right)\right]A_e \\ & -\left\{(\alpha_0\rho_0)_P\xi_w + (\alpha_0\rho_0)_w\bar{\xi}_w\right\}\left[(u_0^*)_w - d_{0w}\left(\left(P_g'\right)_P - \left(P_g'\right)_W\right)\right]A_w \\ & +\left\{(\epsilon_0\rho_0)_N\xi_n + (\epsilon_0\rho_0)_p\bar{\xi}_n\right\}\left[(u_0^*)_n - d_{0n}\left(\left(P_g'\right)_N - \left(P_g'\right)_P\right)\right]A_n \\ & -\left\{(\alpha_0\rho_0)_P\xi_s + (\alpha_0\rho_0)_s\bar{\xi}_s\right\}\left[(u_0^*)_s - d_{0s}\left(\left(P_g'\right)_P - \left(P_g'\right)_S\right)\right]A_s = 0 \end{aligned} \tag{A22}$$

$$a_P\left(P_g'\right)_P = \sum_{nb} a_{nb}\left(P_g'\right)_{nb} + b \qquad a_P = a_E + a_W + a_N + a_S \tag{A23}$$

$$a_E = \left\{(\alpha_0\rho_0)_E\xi_e + (\alpha_0\rho_0)_P\bar{\xi}_e\right\}d_{0e}A_e \qquad a_W = \left\{(\alpha_0\rho_0)_P\xi_w + (\alpha_0\rho_0)_w\bar{\xi}_w\right\}d_{0w}A_w \tag{A24}$$

$$a_N = \{(\alpha_0\rho_0)_N\xi_n + (\alpha_0\rho_0)_p\bar{\bar{\xi}}_n\}d_{0n}A_n \qquad a_S = \{(\alpha_0\rho_0)_P\xi_s + (\alpha_0\rho_0)_s\bar{\bar{\xi}}_s\}d_{0s}A_s \tag{A25}$$

$$\begin{aligned} b = \Bigg\{\left(\frac{(\alpha_0\rho_0)_P - (\alpha_0\rho_0)_P^0}{\Delta t}\right)\Delta V\left[(\alpha_0\rho_0)_E\xi_e + (\alpha_0\rho_0)_P\bar{\bar{\xi}}_e\right]u_{0e}^*A_e \\ - \left[(\alpha_0\rho_0)_P\xi_w + (\alpha_0\rho_0)_w\bar{\bar{\xi}}_w\right]u_{0w}^*A_w + \left[(\alpha_0\rho_0)_N\xi_n + (\alpha_0\rho_0)_p\bar{\bar{\xi}}_n\right]u_{0n}^*A_n \\ - \left[(\alpha_0\rho_0)_P\xi_s + (\alpha_0\rho_0)_s\bar{\bar{\xi}}_s\right]u_{0s}^*A_s\Bigg\} \end{aligned} \tag{A26}$$

The discretization of energy balance equation is similar to that of the scalar transport equation described. The energy equations are coupled because of interphase heat transfer and are partially decoupled with the algorithm described.

Solids volume fraction correction equation

A small change in the solids pressure can be calculated as a function of the change in solids volume fraction:

$$P_m' = K_m\alpha_m' \ , \qquad K_m = \frac{\partial P_m}{\partial \alpha_m} \tag{A27}$$

Denote the solids velocity obtained from the tentative solids pressure field and solids volume fraction field as $(u_m^*)_e$

The actual solids velocity can be represented as

$$(u_m)_e = (u_m^*)_e + (u_m')_e \tag{A28}$$

where the correction $(u_m')_e$ is related to the correction in the solids pressure field as

$$(u_m')_e = e_e[(P_m')_P - (P_m')_E] \tag{A29}$$

Also, the volume fractions can be expressed as a sum of the current value plus a correction

$$(\alpha_m)_e = (\alpha_m^*)_e + (\alpha_m')_e \tag{A30}$$

So, the flux $(\rho_m\alpha_m u_m)_e$ in convection Term can be expressed as

$$\begin{aligned} (\rho_m)_e(\alpha_m)_e(u_m)_e \approx (\rho_m)_e(\alpha_m^*)_e(u_m^*)_e + (\rho_m)_e\left[\bar{\bar{\xi}}_e(u_m^*)_e + (\alpha_m^*)_e(K_m)_P e_e\right](\alpha_m')_P \\ + (\rho_m)_e[\xi_e(u_m^*)_e - (\alpha_m^*)_e(K_m)_E e_e](\alpha_m')_E \end{aligned} \tag{A31}$$

For transient term

$$\begin{aligned} \int\frac{\partial}{\partial t}(\alpha_m\rho_m)_P &= \frac{[(\alpha_m)_P(\rho_m)_P - (\alpha_m)_P^0(\rho_m)_P^0]}{\Delta t}\Delta V \\ &= \frac{[((\alpha_m^*)_P + (\alpha_m')_P)(\rho_m)_P - (\alpha_m)_P^0(\rho_m)_P^0]\Delta V}{\Delta t} \\ &= \frac{(\alpha_m')_P(\rho_m)_P\Delta V}{\Delta t} + \frac{[(\alpha_m^*)_P(\rho_m)_P - (\alpha_m)_P^0(\rho_m)_P^0]}{\Delta t}\Delta V \end{aligned} \tag{A32}$$

Collecting all the terms, a correction equation for volume fraction correction can be written as:

$$a_p(\alpha'_m)_P = \sum_{nb} a_{nb}(\alpha'_m)_{nb} + b \tag{A33}$$

$$a_E = [(\rho_m\alpha_m)^*_e e_e (K_m)_E - \xi_e(\rho_m)_E(u_m)^*_e]A_e \tag{A34}$$

$$a_W = \left[(\rho_m\alpha_m)^*_w e_w (K_m)_W - \bar{\xi}_w(\rho_m)_W(u_m)^*_w\right]A_w$$

$$a_N = \left[(\rho_m\alpha_m)^*_n e_n (K_m)_N - \xi_n(\rho_m)_N(u_m)^*_n\right]A_n \tag{A35}$$

$$a_s = \left[(\rho_m\alpha_m)^*_s e_s (K_m)_S - \bar{\xi}_s(\rho_m)_S(u_m)^*_s\right]A_s$$

$$\begin{aligned} a_P = {} & (\rho_m)_P\left[\bar{\xi}_e(u^*_m)_e A_e - \xi_W(u^*_m)_W A_W + \bar{\xi}_n(v^*_m)_n A_n - \bar{\xi}_s(v^*_m)_s A_s\right] \\ & +(K_m)_P\left[\left(\rho_m\alpha^*_m\right)_e e_e A_e + \left(\rho_m\alpha^*_m\right)_W e_W A_W + \left(\rho_m\alpha^*_m\right)_n e_n A_n + \left(\rho_m\alpha^*_m\right)_s e_s A_s\right] \\ & +(\rho_m)_P\frac{\Delta V}{\Delta t} \end{aligned} \tag{A36}$$

$$\begin{aligned} b = {} & -\left(\rho_m\alpha^*_m\right)_e (u^*_m)_e A_e + \left(\rho_m\alpha^*_m\right)_W (u^*_m)_W A_W \\ & -\left(\rho_m\alpha^*_m\right)_n (v^*_m)_n A_n + \left(\rho_m\alpha^*_m\right)_s (v^*_m)_s A_s \\ & -\left[\left(\rho_m\alpha^*_m\right)_P - \left(\rho_m\alpha^*_m\right)^0_P\right]\frac{\Delta V}{\Delta t} \end{aligned} \tag{A37}$$

Under relaxation

To ensure the stability of the calculations, it is necessary to under relax the changes in the field variables during iterations.

Where $0 \le \omega_\phi \le 1$ when $\omega_\phi = 0$ the old value remains unchanged.

Applying the under relaxation factor first the equations was solved and then applied Under relaxation as because of the better conditioning of the linear equation set and the consequent savings in the solution time.

Calculation of residuals

The convergence of iterations is judged from the residuals of various equations. The residuals are calculated before under relaxation is applied to the linear equation set. The standard form of the linear equation set is

$$a_P\phi_P = b + a_E\phi_E + a_W\phi_W + a_N\phi_N + a_S\phi_S + a_T\phi_T + a_B\phi_B \tag{A39}$$

Denoting the current value as ϕ^*, the residual at point P is given by

$$R_{\phi P} = b + a_E\phi^*_E + a_W\phi^*_W + a_N\phi^*_N + a_S\phi^*_S + a_T\phi^*_T + a_B\phi^*_B - a_P\phi^*_P \tag{A40}$$

Nomenclature

b, C_μ, C_3 C_V, C_β	Coefficients in turbulence model

C_D	Drag coefficient
Cp	Specific heat, J/(kg.k)
d_p	Solid diameter, mm
$Ds, D_{t,sg}$	Turbulent quantities for the dispersed phase
e_{ss}	Coefficient of restitution of particle
g	Gravitational constant, 9.81m/s^{-2}
$g_{0,ss}$	Radial distribution function
$G_{k,g}$	Production of turbulent kinetic energy
H	Expanded bed height, cm
H_0	Static bed height, cm
H_{gs}	Heat transfer between the gas and the solid, J/m^{3}s
I	Turbulent intensity
I_{2D}	Second invariant of the deviatoric stress, s^{-2}
$K_{\theta s}$	Diffusion coefficient for granular energy, Jkg^{-1}
$k^{'}$	Thermal conductivity, J/(m.K.s)
k	Turbulence kinetic energy tensor, dimensionless
$L_{t,g}$	Length scale of the turbulent eddies, m
Nu_s	Nusselt number, dimensionless
p	Pressure, Pa
P_r	Gas Prandtl number, dimensionless
R_e	Reynolds number, dimensionless
S	Modulus of the mean rate-of-strain tensor
T	Time, s
U, V	Superficial gas velocity, m/s
$\overrightarrow{Vi}$	Velocity, m/s
$\overrightarrow{v_{dr}}$	Drift velocity, m/s
$\overrightarrow{V_{s,\|\|}}$	Particle slip velocity parallel to the wall, m/s

Greek symbols

α	Volume fraction, dimensionless
β_{gs}	Gas-solid inter phase exchange coefficient, kgm^{-3}s^{-1}
ε	Turbulence dissipation rate, m^{2}s^{-3}
$\underline{\underline{\varepsilon}}_{s,\max}$	Volume fraction for the particles at maximum packing
τ_x	Reynolds stress tensor, N/m^{-2}
τ_{12}	Particle relaxation time
τ_1^t	Time-scale of turbulent eddies
η_{sg}	Ratio between characteristic times
ϕ_{gs}	Gidaspow's switch function
φ	Angle of internal friction
Θ	Granular temperature, m^{2}s^{-2}
k_{Θ_s}	Diffusion coefficient
φ_{gs}	Transfer of kinetic energy, J/(m^3.s)
γ_{Θ_s}	Collision dissipation of energy, J/(m^3.K.s)

γ_{gs}^{0}	Heat transfer coefficient, J/(m^3.K.s)
$\mu_{t,g}$	Turbulent (or eddy) viscosity, Pa.s
$\prod_{k,g}$, $\prod_{\varepsilon,g}$	Influence of the dispersed phase on the continuous phase
κ	von Karman constant
η_{sg}	Ratio between characteristic times
φ	Specularity coefficient between the particle and the wall
$\tau_{F,sg}$	Characteristic particle relaxation time connected with the inertial effects, s
$\tau_{t,sg}$	Lagrangian integral time scale, s
$\mu_{s,fr}$	Shear viscosity, Pa.s
$\mu_{s,kin}$	Kinematics viscosity, m^2/s
$\mu_{s,col}$	Collisional part of the shear viscosity, Pa.s

Subscripts

g	gas
mf	minimum fluidization
s	solids
w	wall
t	turbulence

9. References

[1] Gidaspow, D., Multiphase Flow and Fluidization, First ed. Academic press, London, 1994.

[2] Kunii, D., Levenspiel ,O., Fluidization Engineering, Second ed. Butterworth-Heinemann, Boston, 1991.

[3] Ranade, V.V., Computational Flow Modeling for Chemical Reactor Engineering, First ed. Academic press, New York, 2002.

[4] Anderson T. B. and Jackson R. A Fluid Mechanical Description of Fluidized Beds. I & EC Fundam., 6,:527-534, 1967.

[5] Grace, J.R., Taghipour, F., Verification and validation of CFD models and dynamic similarity for fluidized beds. Powder Technology , 139, 99–110, 2004.

[6] Bird, R.B., Stewart, W.E., Lightfoot, E.N., Transport Phenomena. seconded. Wiley, New York, 2002.

[7] Nasr.H, Ahmadi.G, The effect of two-way coupling and inter-particle collisions on turbulence modulation in a vertical channel flow, International Journal of Heat and Fluid Flow, 28 ,1507–1517, 2007.

[8] Taghipour, F., Ellis, N., Wong, C., Experimental and computational study of gas–solid fluidized bed hydrodynamics, Chemical Engineering Science, 60, 6857–6867, 2005.

[9] Kaneko Y., Shiojima T., Horio M., DEM simulation of fluidized beds for gas-phase olefin polymerization, Chemical Engineering Science, 54, 5809–5821, 1999.

[10] Rong. F., Marchisio. D.L., Fox. R.O., CFD Simulation of Polydisperse Fluidized-Bed Polymerization Reactors, Department of Chemical Engineering, Iowa State

University, 2114 Sweeney Hall, Ames, IA 50010-2230, USA, Preprint submitted to Elsevier Science, August 2003.

[11] Behjat. Y, Shahhosseini.S, Hashemabadi.S.H, CFD modeling of hydrodynamic and heat transfer in fluidized bed reactors, International Communications in Heat and Mass Transfer, 35, 357–368, 2008.

[12] Gobin, H. Neau, O. Simonin, J. Llinas, V. Reiling, J.L. Selo, Fluid dynamic numerical simulation of a gas phase polymerization reactor, International Journal for Numerical Methods in Fluids, 43,1199–1220, 2003.

[13] Van Wachem, B.G.M., Schouten, J.C., Van den Bleek, C.M., Krishna, R., Sinclair, J.L., Comparative analysis of CFD models of dense gas–solid systems, AIChE Journal, 47, 1035–1051, 2001.

[14] Van Wachem, B.G.M., Schouten, J.C., Van den Bleek, C.M., Krishna, R., Sinclair, J.L., CFD modeling of gas-fluidized beds with a bimodal particle mixture, AIChE Journal, 47, 1292–1302, 2001.

[15] Wachem .V. B.G.M., Schouterf .J.C., Krishnab. R., and Bleek . van den.C.M., Eulerian Simulations of Bubbling Behaviour in Gas-Solid Fluidized Beds, Computers chcm. Engng , 22, 299-306, 1998.

[16] Chiesa, M., Mathiesen, V., Melheim, J.A.., Halvorsen, B., Numerical simulation of particulate flow by the Eulerian–Lagrangian and the Eulerian–Eulerian approach with application to a fluidized bed, Computers & Chemical Engineering, 29, 291–304, 2005.

[17] Mansoori, Z., Saffar-Avval, M., Basirat Tabrizi, H., Ahmadi, G., Modeling of heat transfer in turbulent gas–solid flow, Int. J. Heat Mass Transfer, 45, 1173, 2002.

[18] Mansoori, Z., Saffar-Avval, M., Basirat Tabrizi, H., Ahmadi, G., Lain, S., Thermo-mechanical modeling of turbulent heat transfer in gas–solid flows including particle collisions, Int. J. Heat Fluid Flow, 23, 792, 2002

[19] Saffar-Avval M., Basirat Tabrizi H., Mansoori Z., Ramezani P., Gas–solid turbulent flow and heat transfer with collision effect in a vertical pipe, Int. J. Thermal Sciences 46, 67–75, 2007.

[20] Syamlal, M., O'Brien, T.J., Computer simulation of bubbles in a fluidized bed. A.I.Ch.E. Symposium Series, 85, 22–31,1989.

[21] Syamlal, M., O'Brien, T.J., Fluid dynamic simulation of O3 decomposition in a bubbling fluidized bed. A.I.Ch.E. Journal 49, 2793–2801, 2003

[22] Cao. J., Ahmadi. G.,.Gas–particle two-phase turbulent flow in a vertical duct, Int. J. Multiphase Flows, 21,1203-1228, 1995.

[23] Cao. J., Ahmadi. G., Gas–particle two-phase flow in horizontal and inclined ducts, Int. J. Eng. Sci. 38, 1961-1981, 2000.

[24] Wen, C.-Y., Yu, Y.H.,. Mechanics of fluidization. Chemical Engineering Progress Symposium Series 62, 100–111, 1966.

[25] Abu-Zaid, S., Ahmadi, G., A rate dependent model for turbulent flows of dilute and dense two phase solid-liquid mixtures, powder Technology, 89, 45-56, 1996.

[26] Ding, J., Gidaspow, D., A bubbling fluidization model using kinetic theory of granular flow, A.I.Ch.E. Journal, 36, 523–538, 1990.

[27] Gelderbloom, S.J., Gidaspow, D., Lyczkowski, R.W., CFD simulations of bubbling/collapsing fluidized beds for three Geldart groups. A.I.Ch.E. Journal, 49, 844–858, 2003.

[28] Huilin, L., Yurong, H., Gidaspow, D., Hydrodynamic modeling of binary mixture in a gas bubbling fluidized bed using the kinetic theory of granular flow, Chemical Engineering Science, 58, 1197–1205, 2003.

[29] Lun, C.K.K., and Savage, S.B., A Simple Kinetic Theory for Granular Flow of Rough, Inelastic, Spherical Particles, J. Appl. Mech., 54, 47-53, 1987.

[30] Zhong.W, Zhang.M, Jin.B, Zhang.Y, Xiao.R, Huang.Y, Experimental investigation of particle mixing behavior in a large spout-fluid bed, Chemical Engineering and Processing, 2007.

[31] Zhong.W, Zhang.M, Jin.B, Maximum spoutable bed height of spout-fluid bed, Chemical Engineering Journal, 124, 55–62, 2006.

[32] Gamwo.I.K, Soong.Y, Lyczkowski.R.W, Numerical simulation and experimental validation of solids flows in a bubbling fluidized bed, Powder Technology, 103, 117–129, 1999.

[33] Pain, C., Mansoorzadeh, S., Oliveira, C.R.E.D., Goddard, A.J.H., Numerical modeling of gas–solid fluidized beds using the two-fluid approach, International Journal for Numerical Methods in Fluids, 36, 91–124, 2001.

[34] Du, W., Xiaojun, B.,, Jian, X.,Weisheng,W., computational fluid dynamics (CFD) modeling of spouted bed: influence of frictional stress, maximum packing limit and coefficient of restitution of particles, Chemical Engineering Science, 61, 4558-4570, 2006.

[35] Hui, K., Haff, P.K. and Jackson, R., Boundary Conditions for High-Shear Grain Flows. J.F.M. 145, 223-233, 1984.

[36] Johnson, P.C. and Jackson, R., Frictional-Collisional Constitutive Relations for Granular materials, with Application to Plane Shearing. J. Fluid Mech., 176, , 67-93, 1987.

[37] Patankar, S.V., Numerical heat transfer and fluid flow, First ed. Hemisphere Publishing, Washington, DC, 1980.

[38] Huilin, L., Wentie,L., Feng, L., Guangbo, Z., Huilin, H.L., Wentie, L., Feng, L., Guangbo, Z., Yurong, H., Eulerian simulations of bubble behavior in a two-dimensional gas–solid bubbling fluidized bed, International Journal of Energy Research, 26,1285–1293, 2002.

[39] Syamlal, M., W.A. Rogers, and T.J. O'Brien,. "MFIX Documentation, Theory Guide," Technical Note, DOE/METC-94/1004, NTIS/DE94000087, National Technical Information Service, Springfield, VA, 1993.

[40] Syamlal, M. December. MFIX Documentation: Numerical Techniques. DOE/MC-31346-5824. NTIS/DE98002029. National Technical Information Service, Springfield, VA, 1998

[41] Fluent, Fluent 6.3, User's Guide, 23, Modeling Multiphase Flows and 12, Modeling Turbulence, Fluent Inc, 2006.

[42] Gidaspow, D., Hydrodynamics of Fluidization and Heat Transfer: Supercomputer Modeling, Appl. Mech. Rev., 39, 1-23, 1986.

[43] Fan, R., Marchisio., D.L., Fox. R.O., CFD Simulation of Polydisperse Fluidized-Bed Polymerization Reactors, Department of Chemical Engineering, Iowa State University, 2114 Sweeney Hall, Ames, IA 50010-2230, USA, Preprint submitted to Elsevier Science, August 2003.

[44] Lettieri. P., Saccone. G., Cammarata. L., Predicting the Transition from Bubbling to Slugging Fluidization Using Computational Fluid Dynamics ,Trans IChemE, Part A, 2004 Chemical Engineering Research and Design, 82(A8): 939–944

[45] Algeri, C., Rovaglio, M., Dynamic Modeling of a Poly(ethylene terephthalate) Solid-State Polymerization Reactor I: Detailed Model Development, Ind. Eng. Chem. Res., 43, 4253-4266, 2004.

[46] Rovaglio M., Algeri, C., and Manca, D., Dynamic modeling of a poly(ethylene terephthalate) solid-state polymerization reactor II: Model predictive control, Ind. Eng. Chem. Res., 43, 4267-4277, 2004.

[47] Hamzehei, M., Rahimzadeh, H., Experimental and Numerical Study of Hydrodynamics with Heat Transfer in a Gas-Solid Fluidized bed Reactor at Different Particle Sizes, Ind. Eng. Chem. Res., 48, 3177–3186, 2009.

[48] Hamzehei, M., Rahimzadeh, H., Ahmadi, G., Computational and Experimental Study of Heat Transfer and Hydrodynamics in a 2D Gas-Solid Fluidized Bed Reactor, Ind. Eng. Chem. Res., (Special Issue) 49, 5110–5121, 2010.

[49] Hamzehei, M., Rahimzadeh, H., Ahmadi, G., Studies of gas velocity and particles size effects on fluidized bed hydrodynamics with CFD modeling and experimental investigation, Journal of Mechanics, 26, 113-124, 2010.

[50] Hamzehei, M. and Rahimzadeh, H., Investigation of a Fluidized Bed Chamber Hydrodynamics with Heat Transfer Numerically and Experimentally, Korean Journal of Chemical Engineering, 27, 355.363, 2010.

[51] Hamzehei, M., Rahimzadeh, H., Ahmadi, G., Study of Bed Height and Gas Velocity Effect on Hydrodynamics and Heat Transfer in a Gas-Solid Fluidized Bed Reactor Experimentally and Numerically, Heat Transfer Engineering, 2010, (Accepted).

[52] M., Hamzehei , H., Rahimzadeh, Study of Parameters Effect on Hydrodynamics of a Gas-Solid Chamber Experimentally and Numerically, Proceeding of Experimental Fluid Mechanics Conference, (EFM 2010), Liberec, Czech Republic November 24-26, 2010.

[53] Hamzehei, M., Rahimzadeh, H., Ahmadi, G., CFD Modeling and Simulation of Hydrodynamics in a Fluidized Bed Chamber with Experimental Validation, Proceeding of the *31st* IASTED International Conference on Modelling, Identification, and Control (*MIC* 2011) Innsbruck, Austria, February 14 – 16, 2011

[54] Hamzehei, M., Rahimzadeh., Study of Particle Size Effects on Hydrodynamics of a Fluidized Bed Chamber Experimentally and Computationally, Proceeding of 3rd Technology and Innovation for Sustainable conference (TISD2010) in Nong Khai, Thailand, March 4-6, (Best Paper and best presentation on the Topic E: Energy Technology, Thermal Systems and Applied Mechanics).

[55] Hamzehei, M., Rahimzadeh., Study of Hydrodynamics in a Two phase Fluidized Bed Reactor Experimentally and Numerically, Proceeding of Seventh South African Conference on Computational and Applied Mechanics (SACAM10), Pretoria, January 10–13, 2010.

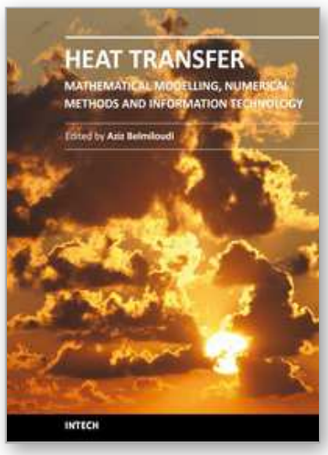

Heat Transfer - Mathematical Modelling, Numerical Methods and Information Technology

Edited by Prof. Aziz Belmiloudi

ISBN 978-953-307-550-1
Hard cover, 642 pages
Publisher InTech
Published online 14, February, 2011
Published in print edition February, 2011

Over the past few decades there has been a prolific increase in research and development in area of heat transfer, heat exchangers and their associated technologies. This book is a collection of current research in the above mentioned areas and describes modelling, numerical methods, simulation and information technology with modern ideas and methods to analyse and enhance heat transfer for single and multiphase systems. The topics considered include various basic concepts of heat transfer, the fundamental modes of heat transfer (namely conduction, convection and radiation), thermophysical properties, computational methodologies, control, stabilization and optimization problems, condensation, boiling and freezing, with many real-world problems and important modern applications. The book is divided in four sections : "Inverse, Stabilization and Optimization Problems", "Numerical Methods and Calculations", "Heat Transfer in Mini/Micro Systems", "Energy Transfer and Solid Materials", and each section discusses various issues, methods and applications in accordance with the subjects. The combination of fundamental approach with many important practical applications of current interest will make this book of interest to researchers, scientists, engineers and graduate students in many disciplines, who make use of mathematical modelling, inverse problems, implementation of recently developed numerical methods in this multidisciplinary field as well as to experimental and theoretical researchers in the field of heat and mass transfer.

InTech Europe
University Campus STeP Ri
Slavka Krautzeka 83/A
51000 Rijeka, Croatia
Phone: +385 (51) 770 447

InTech China
Unit 405, Office Block, Hotel Equatorial Shanghai
No.65, Yan An Road (West), Shanghai, 200040, China
中国上海市延安西路65号上海国际贵都大饭店办公楼405单元
Phone: +86-21-62489820

Fax: +385 (51) 686 166
www.intechopen.com

Fax: +86-21-62489821

IntechOpen

IntechOpen